Simulation of the Aerodynamic Interaction between Rotor and Ground Obstacle Using Vortex Method

Jianfeng Tan
Lecturer
Nanjing Tech University
Nanjing, P.R.China

Yiming Sun
Graduate Student
Nanjing Tech University
Nanjing, P.R.China

Tianyi Zhou
Graduate Student
Nanjing Tech University
Nanjing, P.R.China

George N. Barakos
Professor
University of Glasgow
Glasgow, UK

Richard B. Greeen
Senior Lecturer
University of Glasgow
Glasgow, UK

ABSTRACT

The aerodynamic interaction between rotor wake and surrounding obstacles is complex, and generates high compensatory workload for pilots, degradation of the vehicle handling qualities and performance, and unsteady forces on the structure of the obstacles. The interaction also affects the minimum distance between rotorcraft and obstacles to operate safely. A vortex-based approach is here employed to investigate the complex aerodynamic interaction between rotors and ground obstacles and identify the distance where the interaction ends. This is also one of the objectives of the GARTEUR AG22 effort. In this approach, the aerodynamic loads of the rotor blades are described through a panel method, and the unsteady behavior of the rotor wake is modelled using a vortex particle method. The effects of the ground plane and obstacle are accounted for via a viscous boundary model. The method is then applied to "Large" and "Wee" rotor near the ground and obstacle and compared with earlier experiments carried out at the University of Glasgow. The results show that the predicted rotor induced inflow, and flow-field compare reasonably well with the experiments in terms of magnitude and phase, for the peaks of the radial outwash and vertical downwash. Furthermore, at certain conditions the tip vortices are pushed upwards and are re-ingested into the rotor wake due to the effect of the obstacle resulting in a recirculation. Moreover, contrary to cases without the obstacle, the peak and thickness of the radial outwash near the obstacle is lower due to blockage effects, and an up-wash is observed. Additionally, as the rotor closes to the obstacle, the rotor slipstreams impinge directly on the obstacle, and the up-wash near the obstacle is faster, indicating a stronger interaction between the rotor wake and the obstacle. Also, contrary to the case without the obstacle, the fluctuations of the rotor thrust, roll and pitch moments are obviously strengthened. When the distance between the rotor and the obstacle is larger than 3R, the effect of the obstacle is small.

NOTATION

b, f	=	size of the rectangular panel, m
h_{xi}, h_{yi}, h_{zi}	=	size of the integration cuboid, m
K	=	smooth function, non-dimensional
$\boldsymbol{n}$	=	outward unit normal vector of surface, non-dimensional
p	=	local pressure, Pa
p_{ref}	=	far-field reference pressure, Pa
$\boldsymbol{r}$	=	position vector, m
S_{r}	=	rotor blade surface, m^2
S_{rw}	=	rotor wake surface, m^2
t	=	time, s
$\mathbf{t}$	=	tangential of the body boundary, non-dimensional
$\boldsymbol{u}$	=	fluid velocity, m/s
$\mathbf{u}_{\infty}$	=	free-stream velocity, m/s
$\mathbf{u}_{\text{slip}}$	=	induced velocity from vorticity, m/s
$\boldsymbol{v}_{\text{r}}$	=	velocity of a point on the rotor surface, m/s
$\boldsymbol{v}_{\text{ref}}$	=	referenced velocity of the rotor, m/s
V	=	velocity magnitude, m/s
$\boldsymbol{x_j}$	=	position of particle, m
$\boldsymbol{\alpha}_j$	=	vector-valued vorticity of particle, 1/s
$\boldsymbol{\gamma}$	=	bound vortex sheet, 1/s
ζ_{ε}	=	kernel function, non-dimensional
μ	=	doublet of rotor blades, m^4/s
ν	=	kinematic viscosity, m^2/s
ρ	=	density, kg/m^3
σ	=	source of rotor blades, m^3/s
ϕ	=	velocity potential, m^2/s
$\boldsymbol{\omega}$	=	vorticity of flow field, 1/s
ΔF_k	=	aerodynamic load on the panel, N
ΔS_{k}	=	panel area, m^2
[*ierfc*]	=	integral of error function complement, non-dimensional

INTRODUCTION

Helicopters are frequently operating close to obstacles, such as buildings, ships, and mountains, for search, rescue, and

Presented at the AHS International 74th Annual Forum & Technology Display, Phoenix, Arizona, USA, May 14-17, 2018.

transportation due to their hover, low-speed flight, vertical landing and take-off capabilities. Nevertheless, the aerodynamic interactions between rotorcraft wakes and obstacles not only produce unsteady forces on the obstacles, but also degrade the rotorcraft performance and handling qualities. Furthermore, pilots may experience high workload when operating near obstacles. This situation may endanger helicopters as shown in the International Helicopter Safety Team reports (IHST)[1]. Therefore, understanding the aerodynamic interaction between helicopters and obstacles is an important research subject.

The work presented in this paper stems out of the activities of the GARTEUR Action Group 22 (AG22) that is investigating the interaction of helicopter wakes with ground obstacles. This GARTEUR group brings together researchers performing measurements of helicopter wakes at model scale with numerical analysts aiming to deliver high-fidelity simulations of the complex interactions taking place in these flows. The GARTEUR group is also touching on important operational issues observed by pilots during search and rescue missions, medevac operations or operations in confined areas like restricted helipads on top of buildings or inside compounds.

In the past, several experimental investigations[2-8] have been carried out to study the influence of obstacles on the flow field and performance of rotors. The flow recirculation phenomena for rotors operating near ground and obstacles were firstly studied by Timm through flow visualization[2]. Forces and moments of rotors near the ground or walls were then tested[3]. Furthermore, the effects of the wake of a large upstream object to a nearby rotorcraft was also conducted at the Fluid Mechanics Laboratory (FML), of the NASA Ames Research Center, and focused on the basic fluid mechanics of the aerodynamic interaction between a rotor and a wake[4]. Moreover, the flow field in the vicinity of a helicopter hovering near a hangar was studied at the National Research Council (NRC) Flight Research Laboratory (FRL)[5]. More recently, the effect of the confined area geometry on the aerodynamic performance of a hovering rotor was investigated[6]. Pressure measurements on the obstacle and particle image velocimetry surveys of a rotor near it were implemented to investigate the interference effects of the building model on the helicopter performance under the GARTEUR Action Group 22[7]. As part of that effort, an experimental study, including the rotor induced inflow and flow field between rotors and obstacles, was carried out at the University of Glasgow[8]. The experiments showed that the obstacle had a strong influence on the rotor flow field.

To date, numerical investigations[3-5, 9-12] employed a variety of techniques, ranging from simple blade element vortex methods to Navier-Stokes-based CFD, to study the aerodynamic interaction between rotorcraft wake and obstacles. The aim of the numerical simulations is to find the best method one can use for simulating such flows. A blade element vortex method (BEV), coupled with a simple prescribed wake contraction model, a mirror-imaged ground model, and a linear wake skew estimation, was implemented by Quinliven[4] to deliver efficient results. However, the BEV method was based on flow superposition, and did not predict the recirculation region found in experiments. This is because the aerodynamic interaction is non-linear, and it is very hard to simulate complex interactional phenomena using simple methods[3]. Therefore, CFD methods, coupled with a simpler model for the rotor were developed to revisit the problem. A fully-coupled helicopter/ship dynamic interface tool had been established by coupling the CFD code (PUMA2) and the flight dynamics simulation (GENHEL) to study the interaction between a helicopter wake and a large aircraft hangar structure[9]. It was shown that when the helicopter was operating close to solid structures the rotor wake significantly affected the oncoming airwake, and the situation became more severe when the rotorcraft moved closer to the ground and hangar. Also, a CFD solver coupled with a blade loading model based on Galerkin's method was proposed to study the helicopter-building interaction[3]. The results indicated that the phenomenon of aerodynamic interference intensely disturbed the flow around the helicopter. Moreover, the CFD solver Cobalt, used with the monotone integrated large eddy simulation (MILES) approach, was employed to study the flow field in the vicinity of a helicopter hovering near a vertical face[5]. It was shown that the helicopter downwash dominated the flow field but including the flow over and around the hangar structure was important.

More recently, within the GARTEUR AG22 group several methods have so far been assessed. These include pure Eulerian, grid-based methods, ROSITA[10] and HMB[11], coupled with actuator disk and unsteady actuator disk models, that can resolve with good accuracy the loads on the rotor blades and the near-field of the helicopter but require large grids and CPU time to propagate the helicopter wake away from the rotor. Other approaches, like pure Lagrangian methods, including the unsteady panel method (UPM), that is based on the potential flow equation for representing the blade loads and on free-wake models for resolving the far-wake of the helicopter[12]. Such methods also face difficulties with the required mirror boundary condition and require a certain degree of empiricism in determining the vortex core radius and roll-up. Also, viscous effects are not usually considered.

Given the importance of the problem at hand, there is a need for efficient and accurate methods that do not suffer from the aforementioned problems but can be used by engineers routinely to find out safe distances to be kept between helicopters and buildings, and support guidelines for pilots regarding the effects of the wake on the surrounding infrastructure. Such methods may need to be developed further if a complete analysis of the wake/obstacle interaction is needed. Here, a vortex particle method, coupling with a viscous boundary model, was developed to numerically investigate the interference between a building, simplified as a cubic box, and a helicopter. In this method, the aerodynamics of the rotor was described through an unsteady panel method, and the unsteady behavior of the vortices near the ground and obstacle was modelled through the viscous vortex particle method[13]. The viscous effects of the ground and obstacle were accounted for by the viscous boundary model

satisfying the no-slip and non-pentation boundary conditions. This was implemented by generating a vortex sheet on the ground and obstacle surface and diffusing the vortex into flow field. The flow-field between the rotor and obstacle was then computed and compared with experimental data to validate the present method. The result compared well with the Glasgow University data[8]. The numerical results were performed to investigate the physical interpretation of the aerodynamic interaction between the rotor and ground obstacles, and further explored to the minimum distance from the obstacle to minimize the effect of the obstacle, which is smaller than the clearance, 3 rotor diameters, from taxiing helicopter in the currently established guidance CAP 493[14].

COMPUTATIONAL METHOD

Aerodynamic Model of Rotor

A helicopter has a distinct trailed wake with its own characteristics near the ground and obstacles. This is because the flow-field, especially at low high, is dominated by the wake of rotors. Furthermore, successful aerodynamic analysis of rotorcraft near the ground and obstacles requires accurate modelling of blade airloads and their vortices. The aerodynamics of the rotor is firstly represented by an unsteady panel method[13]. Based on this method, the velocity potential of the rotor is defined in a global reference system (X, Y, Z) in Fig.1, which shows the position of the rotor hub center with respect to the ground and the obstacle, as

$$\phi(x,y,z,t)=\frac{1}{4\pi}\int_{S_r}\mu\boldsymbol{n}\cdot\nabla(\frac{1}{r})dS -\frac{1}{4\pi}\int_{S_r}\sigma(\frac{1}{r})dS+\frac{1}{4\pi}\int_{S_{rw}}\mu\boldsymbol{n}\cdot\nabla(\frac{1}{r})dS \quad (1)$$

where σ and μ are the source and doublet distributions placed on the rotor blades (S_r) and on the wake surface (S_{rw}). $\boldsymbol{n}$ denotes the outward unit normal vector of surfaces, and $\boldsymbol{r}$ is the position vector (x, y, z).

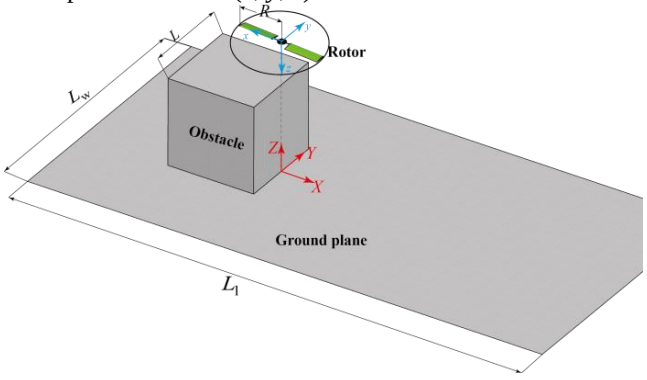

Fig.1 Schema of rotor, ground, and obstacle

The boundary conditions for the rotor require that the velocity component normal to the blades is zero. The boundary conditions at infinity require flow disturbances to decrease to zero. Both can then be expressed as:

$$\begin{cases}\dfrac{\partial\phi}{\partial n}-\boldsymbol{v}_r\cdot\boldsymbol{n}=0 & \text{rotor surface}\\ \lim\nabla\phi_{r\to\infty}=0 & \text{far-field boundary}\end{cases} \quad (2)$$

where $\boldsymbol{v}_r$ is the velocity of a point on the rotor surface S_r.

The boundary condition at infinity is automatically fulfilled through Green's function[13]. According to the Neumann boundary condition, and the trailing-edge Kutta condition, the surface boundary conditions are transformed to algebraic equations that are solved for the source and doublet distributions. The flow-field of the rotor is then determined, and based on the panel method as mentioned before, the unsteady pressure on the rotor blade surfaces can be calculated using the velocity potential and flow velocity through Bernoulli's equation. Thus, the non-dimensional form of the blade unsteady pressure is then given as:

$$C_p=\frac{p-p_{\text{ref}}}{(1/2)\rho(\boldsymbol{v}_{\text{ref}})^2}=1-\frac{(\boldsymbol{v})^2}{(\boldsymbol{v}_{\text{ref}})^2}-\frac{2}{(\boldsymbol{v}_{\text{ref}})^2}\frac{\partial\phi}{\partial t} \quad (3)$$

where p_{ref} and ρ are far-field referenced pressure and density, $\boldsymbol{v}$, p, $\boldsymbol{v}_{\text{ref}}$ are the local fluid velocity, local pressure, referenced velocity, respectively, at each section of the rotor. ϕ is the velocity potential.

The aerodynamic forces on the panels of the rotor can then be computed as:

$$\Delta\boldsymbol{F}_k=-C_{pk}\left(\rho\boldsymbol{v}_{\text{ref}}^2/2\right)_k\Delta S_k\boldsymbol{n}_k \quad (4)$$

where $\Delta\boldsymbol{F}_k$ is the aerodynamic load on the panel, ΔS_k is the panel area, and $\boldsymbol{n}_k$ is its normal vector.

Wake Model of the Rotor

The tip vortex emanating from the blade needs to be preserved for over long time to capture the interaction with the ground and the obstacle. So, the wake of rotor is modelled based on the viscous vortex particle method[13] which solves the Navier-Stokes equation with velocity-vorticity ($\boldsymbol{u}$, $\boldsymbol{\omega}$) in Lagrangian frame using vector-valued particles.

$$\frac{\partial\boldsymbol{\omega}}{\partial t}+\boldsymbol{u}\cdot\nabla\boldsymbol{\omega}=\nabla\boldsymbol{u}\cdot\boldsymbol{\omega}+\nu\nabla^2\boldsymbol{\omega} \quad (5)$$

where ν is the kinematic viscosity, and $\boldsymbol{\omega}=\nabla\times\mathbf{u}$ is the vorticity field associated with the velocity field.

The second term on the left hand-side describes the vortex particle convection which is solved using the fourth-order Runge-Kutta scheme with the Biot-Savart law. The right hand-side includes the vortex particle stretching and viscous diffusion effects. Viscous diffusion ($\nu\nabla^2\boldsymbol{\omega}$) is simulated through the Particle Strength Exchange (PSE) which suggests that the Laplacian operator ∇^2 can be replaced by an integral operator [15, 16] as:

$$\nabla^2\boldsymbol{\omega}\approx\frac{2}{\varepsilon^2}\int_V\zeta_\varepsilon(\mathbf{x}-\mathbf{y})[\boldsymbol{\omega}(\mathbf{x})-\boldsymbol{\omega}(\mathbf{y})]d\mathbf{y} \quad (6)$$

where ζ_ε is a kernel function with Gaussian distribution, and ε is the smoothing radius.

Vortex stretching ($\nabla\mathbf{u}\cdot\boldsymbol{\omega}$) is represented by a direct scheme where the velocity gradient can be expressed as a

product of the kernel function gradient and the position gradient[17]. Thus, the particle velocity gradient in Eq. (5) can be expressed as follows:

$$\nabla \mathbf{u}(\mathbf{x},t) = -\sum_{j=1}^{N} \nabla[K_\varepsilon(\rho)(\mathbf{x}-\mathbf{x}_j)] \times \boldsymbol{\alpha}_j \tag{7}$$

where K_ε is the Biot-Savart kernel for velocity evaluation; $\boldsymbol{x}_j$ and $\boldsymbol{\alpha}_j$ are the position and vector-valued vorticity, respectively.

Vortices are shed from the blade surfaces via the applied Neumann boundary condition and by converting shed-wake doublet panels to vorticity[13].

Viscous Model of the Ground and Obstacle

It is believed that having the no-slip and non-pentation boundary conditions is critical to the aerodynamic computation of rotorcraft near the ground and obstacles. Therefore, a viscous boundary model, suitable for complex geometries, such as ground and buildings, is developed by considering the no-slip and non-pentation boundary conditions based on a vorticity sheet concept [18-20].

When a set of bodies, such as the ground and obstacles, is immersed in a flow, its effect can be summarized in two expressions of the boundary conditions: the flow cannot go through solid walls, which is a non-pentation boundary condition, and the tangential velocity of the flow on wall is zero, which is a no-slip boundary condition. They are expressed as,

$$\begin{cases} \mathbf{u}(\mathbf{x}) \cdot \mathbf{n} = 0 & \text{non-pentation boundary condition} \\ \mathbf{u}(\mathbf{x}) \cdot \mathbf{t} = 0 & \text{no-slip boundary condition} \end{cases} \tag{8}$$

where $\mathbf{u}$, $\mathbf{n}$ and $\mathbf{t}$ represent velocity, unit vectors normal and tangential to the body boundary, respectively.

Also, there is a free-stream velocity at the far-field which is written as

$$\mathbf{u}\big|_{\mathbf{x}\to\infty} = \mathbf{u}_\infty \tag{9}$$

Based on the Poincaré's formula[17], a Fredholm equation of the second kind that justifies the no-slip condition can be written as

$$\left[\frac{\boldsymbol{\gamma} \times \mathbf{n}}{2} - \int_S K(\mathbf{x}-\mathbf{x}') \times \boldsymbol{\gamma}(\mathbf{x}') dS \right] \cdot \mathbf{t} = \mathbf{u}_{\text{slip}} \cdot \mathbf{t} \tag{10}$$

where $\mathbf{u}_{\text{slip}}$ is the induced velocity from the vorticity in the flow field. $\boldsymbol{\gamma}$ is bound vortex sheet which enforces the no-slip condition, and K is smooth function,

$$K(\mathbf{x},\mathbf{x}') = -\frac{1}{|\mathbf{x}-\mathbf{x}'|^3} g_3(\rho) \tag{11}$$

where $\rho = |\mathbf{x}-\mathbf{x}'|/\sigma$.

Eq.(10) defines the vortex sheet on the ground surface and on the obstacle which is used to generate vorticity into flow-field. Furthermore, the tangential and normal velocity conditions are satisfied for the non-rotating ground and obstacles based on the stream function related to the vorticity field. The vector sheet, $\boldsymbol{\gamma}$, is parallel to the body surface, hence only two vorticity components need to be determined. By dividing the body surface into vortex sheet panels, integration on the surfaces using Eq. (10) can be equivalently written as the superposition of integrations on the panels constituting those surfaces. Quadrilateral geometry, constant-strength panels are used in the current study. Therefore, the viscous boundary conditions are transformed to algebraic equations that provide the vector vortex sheet distribution.

In a viscous flow, the presence of a solid boundary affects the flow by forcing the fluid to decelerate to zero velocity at the wall. In other words, the solid body is a source of vorticity, and this can be modelled by a flux of vorticity on the body surface[18-22]. Therefore, after a vortex sheet on the boundary is obtained to satisfy the no-slip boundary condition, transferring the vorticity of the vortex sheet to the nearby particles in the fluid domain is carried out. This is accomplished by solving a diffusion equation with the correct boundary conditions:

$$\begin{aligned} &\frac{\partial \boldsymbol{\omega}}{\partial t} - \nu \Delta \boldsymbol{\omega} = 0 \\ &\boldsymbol{\omega}(t - \delta t) = 0 \\ &\nu \frac{\partial \boldsymbol{\omega}}{\partial n} = \frac{-\boldsymbol{\gamma}(s)}{\delta t} \end{aligned} \tag{12}$$

The solution of Eq.(12) can be computed in integral form[18].

$$\boldsymbol{\omega}(\mathbf{x},t) = \int_0^t \int_S G(\mathbf{x},t;\mathbf{s},\tau) \boldsymbol{\gamma}(\xi,\tau) ds d\tau \tag{13}$$

where G is the three-dimensional heat kernel, with $\tau < t$

$$G(\mathbf{x},t;\mathbf{s},\tau) = (4\pi\nu(t-\tau))^{-3/2} \exp\left(-\frac{|\mathbf{x}-\mathbf{s}|^2}{4\nu(t-\tau)}\right) \tag{14}$$

This flux must be emitted during a time Δt. In effect, the vortex sheet $\boldsymbol{\gamma}$ must be distributed to neighboring particles by discretizing Green's integral for the inhomogeneous Neumann problem corresponding to the diffusion equation. Then, a particle receives, from that panel, an amount of "vorticity × volume" given by

$$\Delta \boldsymbol{\alpha}_i = \int_0^{\Delta t} \frac{d\boldsymbol{\alpha}_i}{dt} dt \tag{15}$$

where

$$\frac{d\boldsymbol{\alpha}_i}{dt} = \int_{x_i - h_{xi}/2}^{x_i + h_{xi}/2} \int_{y_i - h_{yi}/2}^{y_i + h_{yi}/2} \int_{z_i - h_{zi}/2}^{z_i + h_{zi}/2} \frac{d\boldsymbol{\omega}}{dt} dx dy dz \tag{16}$$

where (x_i, y_i, z_i) and (h_{xi}, h_{yi}, h_{zi}) are the positions of the particles and the size of the integration cuboid, respectively.

The rate of change of the vorticity, $d\boldsymbol{\omega}/dt$, due to the rectangular panel of uniform strength $\boldsymbol{\gamma}$ and size $b \times f$, is shown in Fig.2, and is equal to

$$\begin{aligned} \frac{d}{dt}\boldsymbol{\omega}(\mathbf{x},t) = &\frac{\Delta\boldsymbol{\gamma}}{\Delta t} \frac{1}{2\sqrt{\pi}} \frac{1}{\sqrt{4\nu t}} \exp\left(-\frac{z^2}{4\nu t}\right) \\ &\left[erfc\right]_{(x-b/2)/\sqrt{4\nu t}}^{(x+b/2)/\sqrt{4\nu t}} \left[erfc\right]_{(y-f/2)/\sqrt{4\nu t}}^{(y+f/2)/\sqrt{4\nu t}} \end{aligned} \tag{17}$$

Then

$$\frac{d\boldsymbol{\alpha}_i}{dt}=\frac{\Delta\gamma}{\Delta t}\left[erfc\right]_{(z_i+h_{zi}/2)/\sqrt{4\nu t}}^{(z_i-h_{i,l}/2)/\sqrt{4\nu t}} \times\frac{1}{2}\sqrt{4\nu t}\left(\left[ierfc\right]_{((x_i-b/2)-h_{xi}/2)/\sqrt{4\nu t}}^{((x_i-b/2)+h_{xi}/2)/\sqrt{4\nu t}}-\left[ierfc\right]_{((x_i+b/2)-h_{xi}/2)/\sqrt{4\nu t}}^{((x_i+b/2)+h_{xi}/2)/\sqrt{4\nu t}}\right) \times\frac{1}{2}\sqrt{4\nu t}\left(\left[ierfc\right]_{((y_i-f/2)-h_{yi}/2)/\sqrt{4\nu t}}^{((y_i-f/2)+h_{yi}/2)/\sqrt{4\nu t}}-\left[ierfc\right]_{((y_i+f/2)-h_{yi}/2)/\sqrt{4\nu t}}^{((y_i+f/2)+h_{yi}/2)/\sqrt{4\nu t}}\right) \quad (18)$$

The time integral in Eq. (15) is evaluated numerically using a Gauss quadrature with four points.

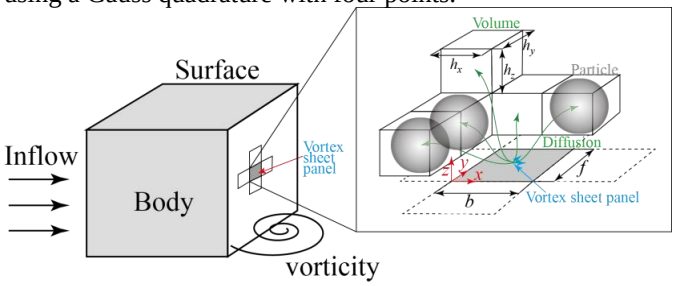

Fig.2 Vortex sheet panel diffusion to particle

NUMERICAL RESULTS AND DISCUSSION

Induced Inflow of the Rotor-Ground-Obstacle

The experiment campaign of Zagaglia et al.[8] conducted at the University of Glasgow is used for verification of the method. The experimental campaign consisted of a set of tests reproducing rotor hover conditions at different positions with respect to a simplified obstacle with a cubic shape. The large rotor rig consisted of four rectangular blades was used to compute rotor induced inflow under the interaction of the ground and obstacle as shown in Fig.3 and Table.1. The rotor inflow measurements along the rotor *x* and *y* axes, 4 cm (4%*D*) above the rotor plane, were carried out by means of a Dantec 2D FiberFlow two-component Laser Doppler Anemometry (LDA) system. The computational blade was modelled with 4800 panels composed of 60 panels in the chordwise direction and 20 panels in the span-wise direction, and the azimuthal angle step was 5.0°. The ground plane and cubic obstacle were resolved using 7600 panels of 5m×3m and 1m×1m, respectively. The rotor was moved with the global reference system (*X*, *Y*, *Z*) which defined the position of the rotor hub centre with respect to the obstacle shown in Fig.3. The origin of the global reference system was fixed and placed on the ground plane at the obstacle mid-span.

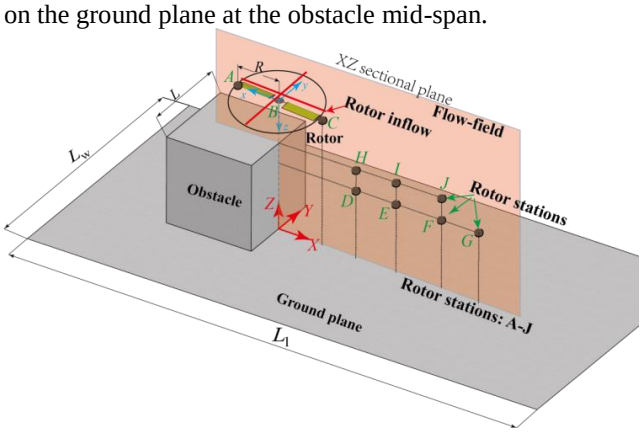

Fig.3 Model of rotor, ground plane and obstacle

Table. 1 Main features of the rotor rigs

Characteristics	"Large" rotor rig	"Wee" rotor rig
Cubic obstacle size	1m	0.3m
Diameter	1m	0.3
Number of blades	4	2
Blade chord	53mm	31.7mm
Solidity	0.135	0.134
Collective pitch	8°	8°
Rotational frequency	1200RPM	4000RPM
Tip Mach number	0.18	0.18

Comparisons of the induced velocity profiles along *X* and *Y* directions at various rotor positions (A-G), *X*/*R*=-1.0, 0.0, 1.0, 1.5, 2.0, 4.0, *Z*/*R*=1.5, 3.0, and no-obstacle, with experiment are shown in Figures 4 and 5. It is shown that the predicted induced velocities have the similar trend as the experiment, and the predicted peak values are found to match very well with the experiment data. Furthermore, the rapid change of downwash near the blade tip (Figures 4 and 5) shows that the effect of tip vortex which is captured by the present method. However, the velocity at the root of the blade is over-predicted since the rotor hubs and the shafts of the test rigs are not modelled in the present work. It should be noted that even if there are small discrepancies, the overall comparison of the induced velocity prediction with the experiments is still very good.

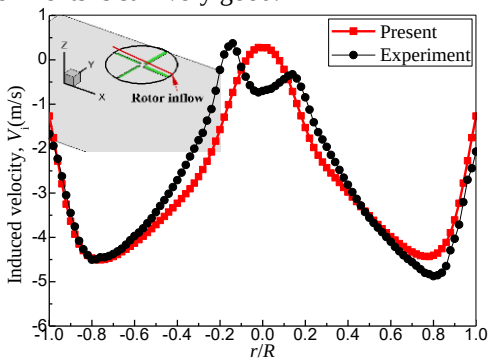

(a) *X* direction (no-obstacle)

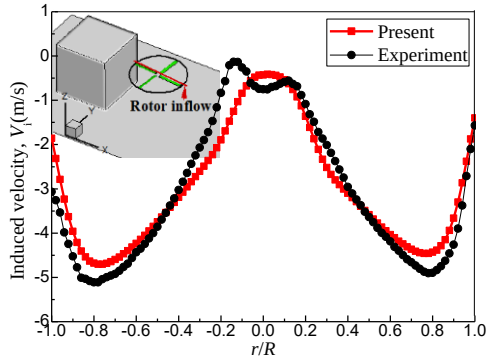

(b) *X* direction (*X*=1.5*R*)

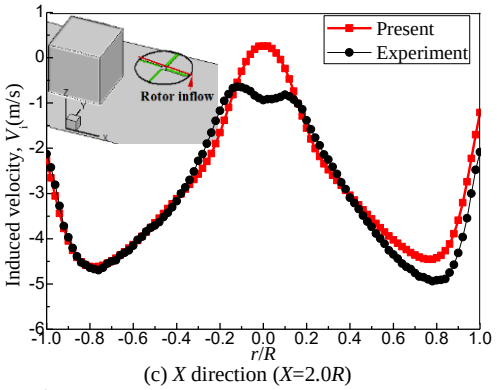

(c) *X* direction (*X*=2.0*R*)

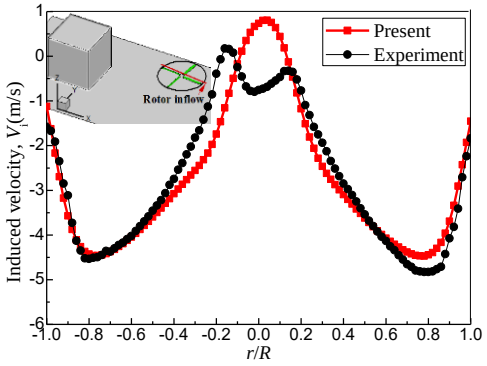

(d) *X* direction (*X*=4.0*R*)

Fig. 4 Induced velocity 4cm (4%*D*) above the rotor plane in *X* direction. The rotor in Fig.4 (b), (c), and (d) are located at stations D (*X*=1.5*R*, *Z*=1.5*R*), E (*X*=2.0*R*, *Z*=1.5*R*), and G (*X*=4.0*R*, *Z*=1.5*R*), respectively.

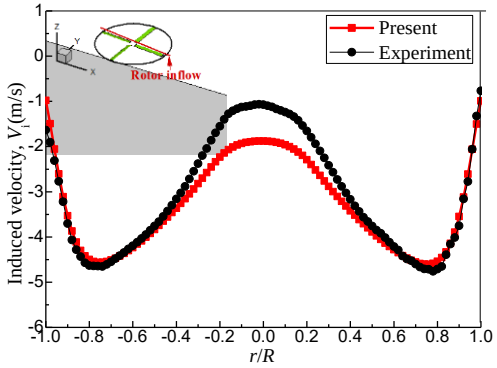

(a) *X* direction (no-obstacle)

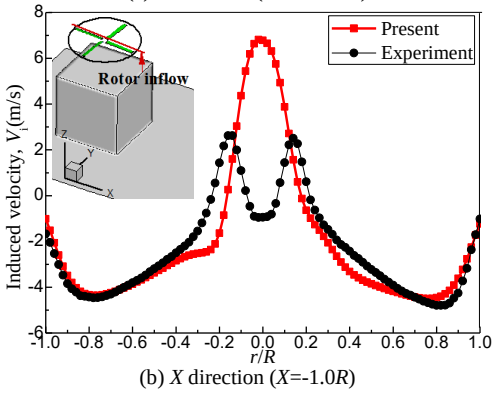

(b) *X* direction (*X*=-1.0*R*)

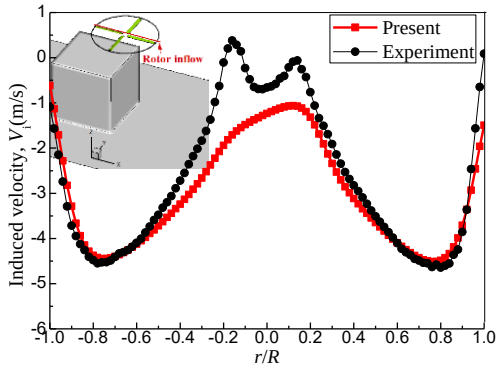

(c) *X* direction (*X*=0.0*R*)

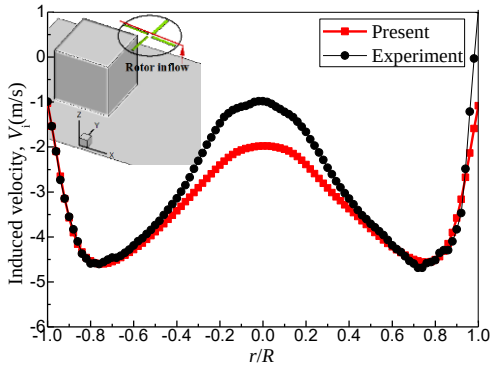

(d) *X* direction (*X*=1.0*R*)

Fig. 5 Induced velocity 4cm (4%*D*) above the rotor plane in *X* direction. The rotor in Fig.5 (b), (c) and (d) are located at stations A (*X*=-1*R*, *Z*=3*R*), B (*X*=0*R*, *Z*=3*R*), and C (*X*=1*R*, *Z*=3*R*), respectively.

The influence of the rotor's position on the induced velocity is shown in Fig.6 that provides some insight into the interaction between the rotor and the ground obstacle. Contrary to the no-obstacle, the peak of the induced velocity of *X*=1.5*R* and *Z*=1.5*R* is clearly larger. This is because the rotor wake impinges upon the obstacle and re-enters the rotor resulting in a recirculation which is confirmed later in Fig.25. Furthermore, the peak induced velocity decreases with increasing the distance between the rotor and the obstacle since this weakens the interaction. However, as opposed to the *Z*=1.5*R* case, the peak induced velocity at *Z*=3.0*R* increases with increasing the distance between the rotor and the obstacle. This is shown in Fig.6(b) that the induced velocity at *X*=-1.0*R* is smaller than for the no-obstacle case. This is because, the rotor is above the obstacle, and the effect of the obstacle is similar to the effect of the ground as confirmed in Fig.7(a). Also, the rotor is above the ground at *X*=1.0*R*, as a result, the rotor wake convects downstream on the starboard side of the obstacle as shown in Fig.7(e), and the effect of the obstacle is weakened.

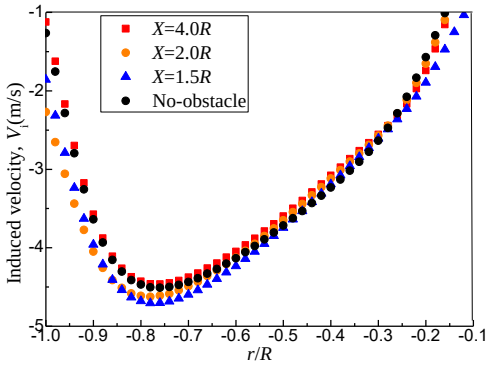

(a) Z=1.5R

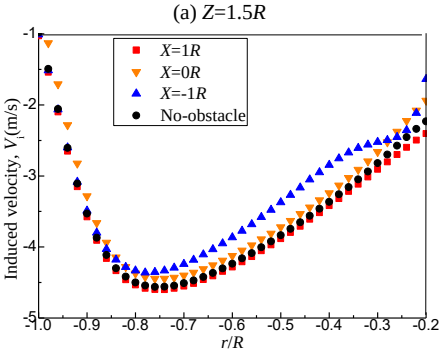

(b) Z=3.0R

Fig. 6 Influence of the rotor's position on the induced velocity 4%D above the rotor in X direction

The wake structure under the interaction with the ground and obstacle at Z=3.0R is plotted in Fig.7. It is shown that at X=-1.0R, Fig.7(b), the rotor tip vortices first contract radially and then expand as they approach the top surface of the obstacle, twine around the obstacle, and finally expand again as they approaching the ground. Furthermore, the vortices convect away from the four sides of the obstacle after impinging upon its top surface. The blade root vortices are pushed up producing a fountain. Like the previous case, the tip vortices on side A at X=0R, Fig.7(d), expand as they approach the top surface of the obstacle and convect far away from the it. However, contrary to the previous case, the tip vortices on side B contract radially, convect downstream as out of ground effect, and then expand as they approach the ground plane. Consequently, the rotor wake twines parts the obstacle. Clearly, as opposed to the previous two cases, since the rotor is located in the upper-right, X=1.0R, the rotor wake is not expand around the obstacle in Fig.7(f). The tip vortices on the side A contract radially, convect downstream, and stay in the area between the obstacle and the ground. Nevertheless, the vortices on the side B expand away from the obstacle as they approach the ground plane and result in a wall jet.

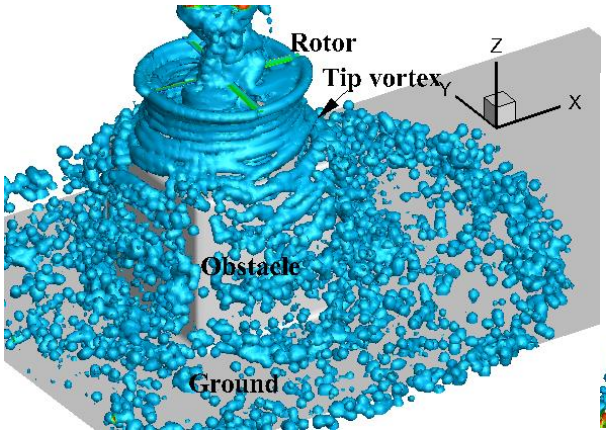

(a) Wake structure (X=-1R)

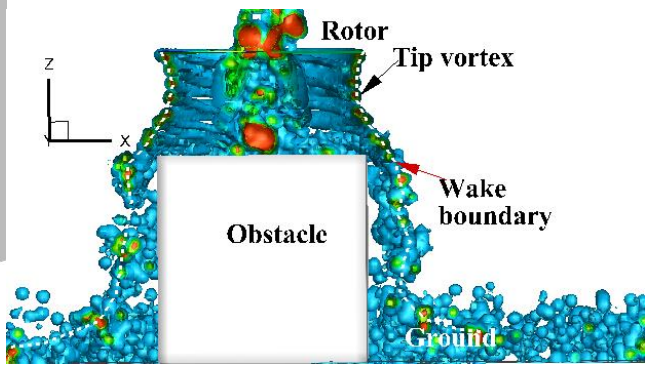

(b) Sectional wake structure (X=-1R)

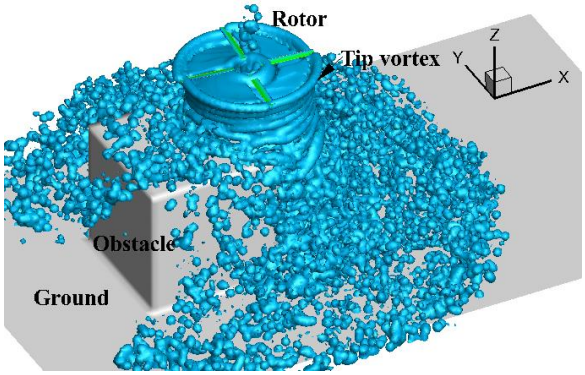

(c) Wake structure (X=0R)

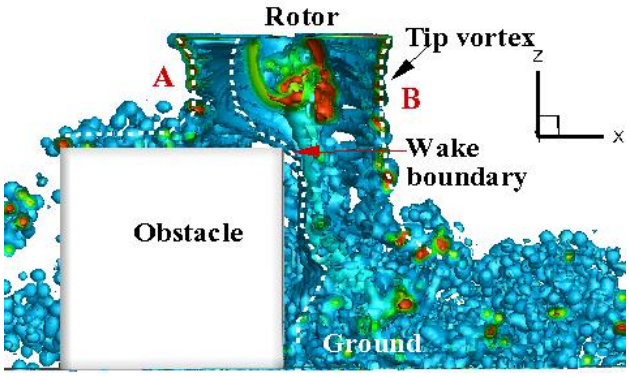

(d) Sectional wake structure (X=0R)

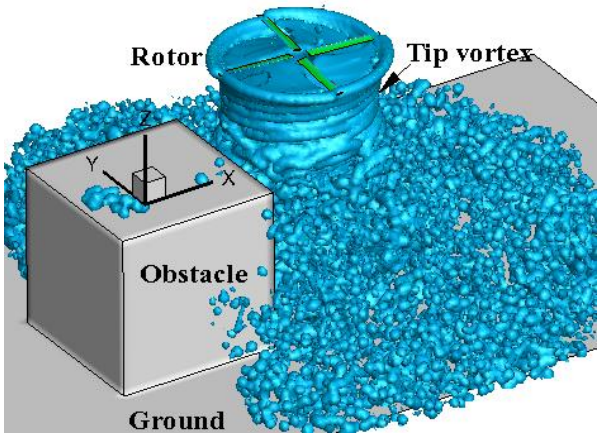

(e) Wake structure (X=1R)

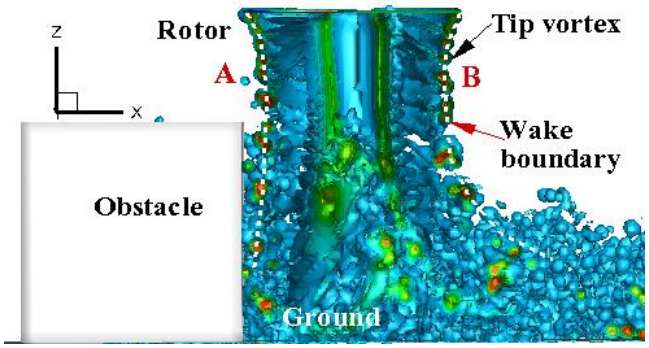

(f) Sectional wake structure (X=1R)

Fig. 7 Wake structure of rotor-ground-obstacle

Flow field of the Rotor-Ground-Obstacle

The flow field for the interaction of the rotor and the ground obstacle is computed based on the "Wee" rotor rig as shown in Tab.1 and Fig.3. The flow field in the region between the obstacle and the rotor was investigated with Stereoscopic PIV[8]. The rotor blade was modelled using 2400 panels composed of 60 panels in the chordwise direction and 20 panels in the span-wise direction, and the azimuthal angle step was 5.0°. The ground plane and the cubic obstacle are modelled using 1900 panels of 0.6m×1.65m and 0.3m×0.3m, respectively.

The predicted velocity contours for the rotor at Z=2.0R, X=1.5R are shown and compared with experimental data in Fig. 8. The comparison demonstrates excellent correlation between the computational predictions and the experimental measurements of the flow field in terms of magnitude and phase. Also, the peak velocity within the wake boundary and the radial outward expansion of the rotor-induced flow are predicted correctly. Furthermore, a recirculation region near the obstacle is also observed.

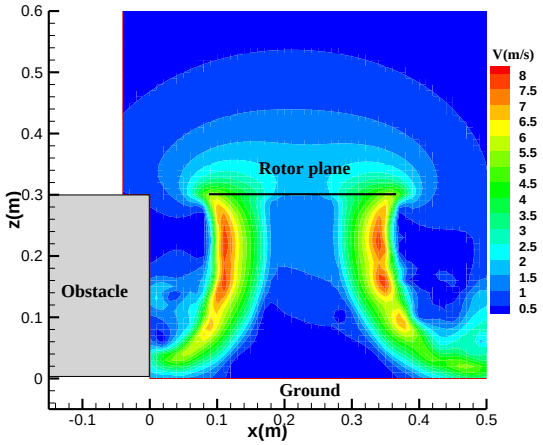

(a) Prediction

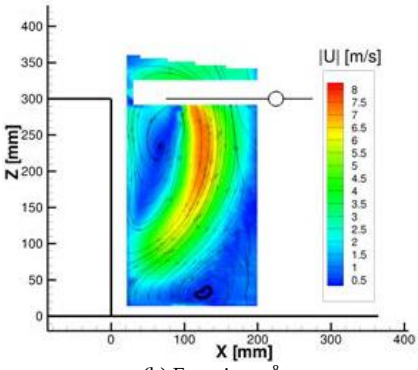

(b) Experiment[8]

Fig.8 In-plane velocity magnitude contours of rotor at Z=2.0R, X=1.5R

A more quantitative validation of the present method compares the time-averaged radial and vertical velocity profiles at different locations (X=0.06m, 0.1m, 0.19m, Z=0.09m, 0.1m, 0.3m, 0.18m, 0.24m, and 0.3m) with the experimental data as shown in Fig.9. The companions are at the rotor plane, contraction, expansion, outwash, downwash, and recirculation regions.

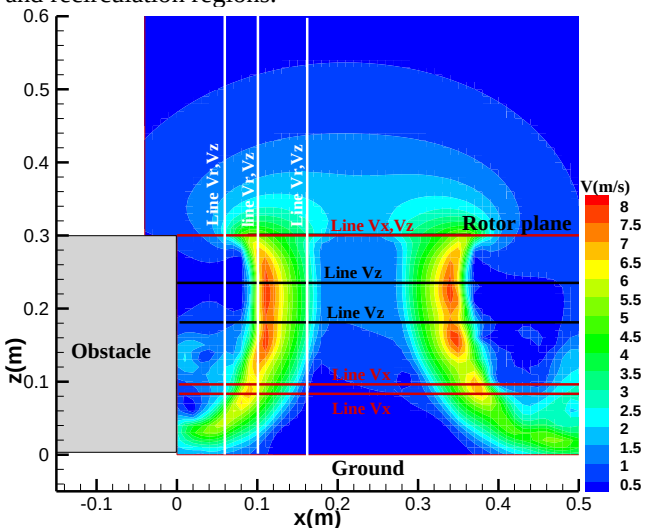

Fig.9 Lines of the velocity parallel and normal to the ground

The extracted horizontal velocities at various downstream distances, Z=0.09m, 0.1m, and 0.3m, across the rotor disc for this configuration are shown in Fig.10. Also, experimental data is used to validate the present approach. At the Z=0.09 and 0.1m, where the flow intensely expands, the predicted horizontal velocity distributions are found to match very well with experiments. Furthermore, even though the position corresponding to the peak velocity is slightly over-predicted, the peak of the outwash velocity is accurately predicted by the present method. Moreover, at Z=0.3m, at the rotor plane, the rotor inflow is predicted correctly.

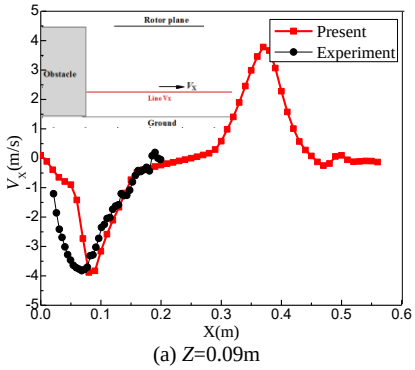

(a) Z=0.09m

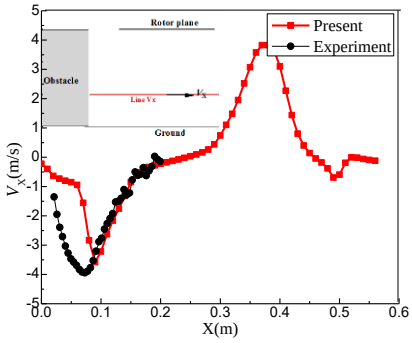

(b) Z=0.1m

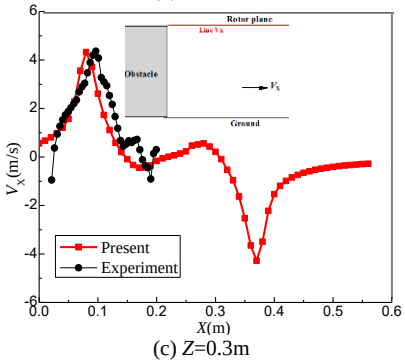

(c) Z=0.3m

Fig.10 Comparison of V_X velocity distribution parallel to the ground

Comparisons of the vertical component of the downwash velocity above the ground plane with experiments are shown in Fig.11. The predicted peak of the downwash velocity and the peak position agree well with the measurements. Furthermore, the rapid changes of the downwash near X=0.1m (Figure 11) show the effect of the tip vortex that is also captured well. It is worth noting that the up-wash velocity near the obstacle (X=0.0m-0.075m), Fig. 11(a), caused by the effect of the obstacle also correlates well with the measured data, indicating that the recirculation region is captured by the present method.

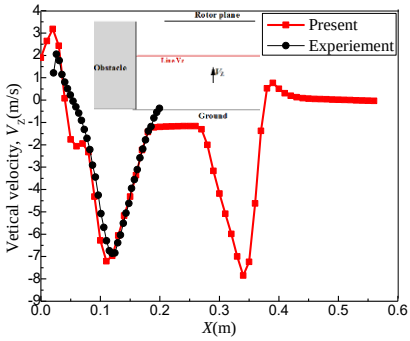

(a) Z=0.18m

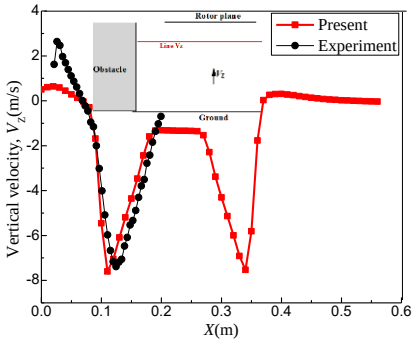

(b) Z=0.24m

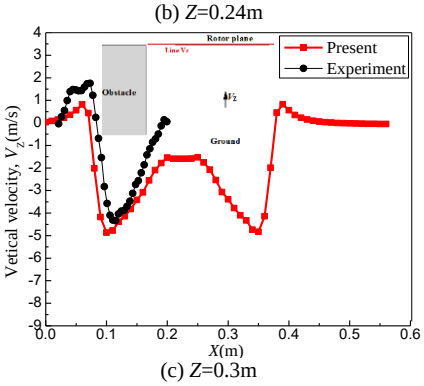

(c) Z=0.3m

Fig.11 Comparison of V_Z velocity distribution parallel to the ground

The predicted radial and vertical velocity components, V_r and V_Z, are plotted against the normal distance from the ground at several radial stations and compared with the experimental data in Figures 12 and 13. It can be seen that, in general, the predicted outwash velocity profiles have a similar trend as the experiment measurements. Furthermore, although the distance above the ground plane corresponding to the peak radial velocity is under-predicted (53.2% difference), the peak radial velocity near the obstacle is predicted reasonably well, which indicates that the outwash due to the ground and obstacle is captured. Additionally, there is good agreement between the computational downwash velocity profiles and the experiments. The downwash velocity at X=0.06m and 0.1m is slightly over-predicted, while it at X=0.16m is under-predicted. Even though there are small discrepancies, the simulation shows acceptable agreement with the test data.

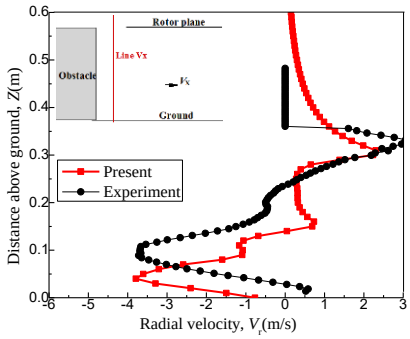

(a) X=0.06m

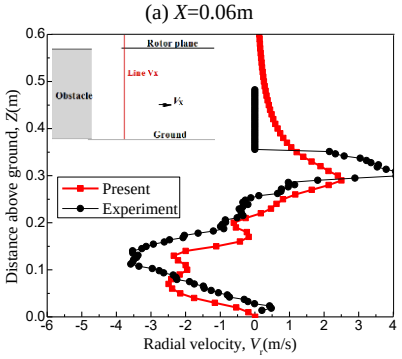

(b) X=0.10m

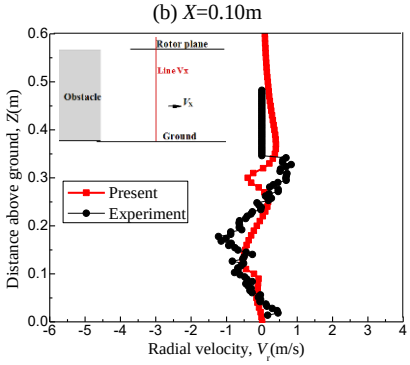

(c) X=0.16m

Fig.12 Comparison of V_r velocity profiles normal to the ground

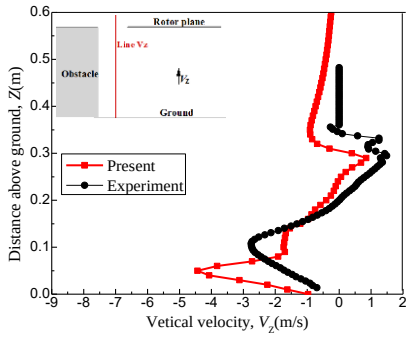

(a) X=0.06m

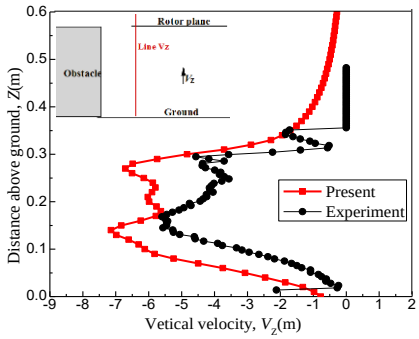

(b) X=0.10m

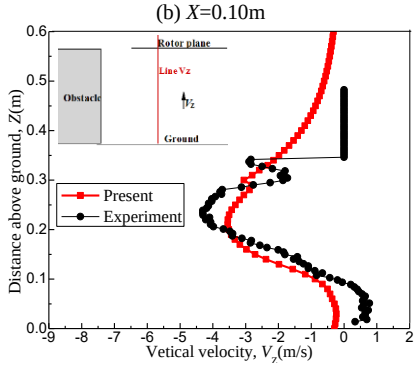

(c) X=0.16m

Fig.13 Comparison of V_Z velocity profiles normal to the ground

Difference of Flow-Field on Both Sides of the Rotor

Figure 14 shows the time average flow field at the XY plane on both sides of the rotor. At the rotor plane and near the ground, the inflow and outwash in the regions A and B are similar as shown in Fig.14(a). However, as opposed to the region B, near the obstacle, the horizontal velocity changes from negative to positive indicating a recirculation. Furthermore, contrary to the region B, the positive vertical velocity is greater, suggesting up-wash near the obstacle as shown in Fig.14(b). Additionally, the velocity along Y axis in the region B is positive due to the swirl resulting from the rotation. Conversely, in the region A near the obstacle, it changes from negative to positive, indicating that there is a recirculation along the X axis.

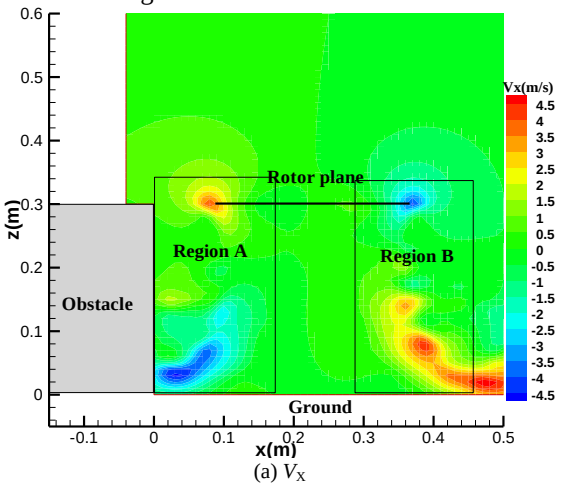

(a) V_X

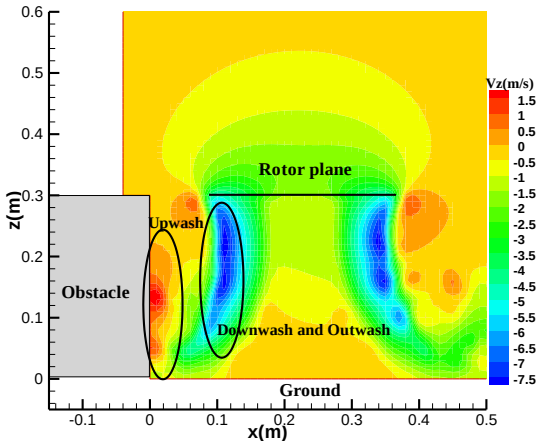

(b) V_Z

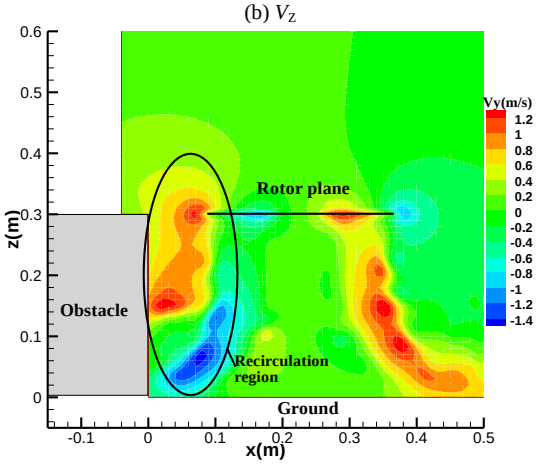

(c) V_Y

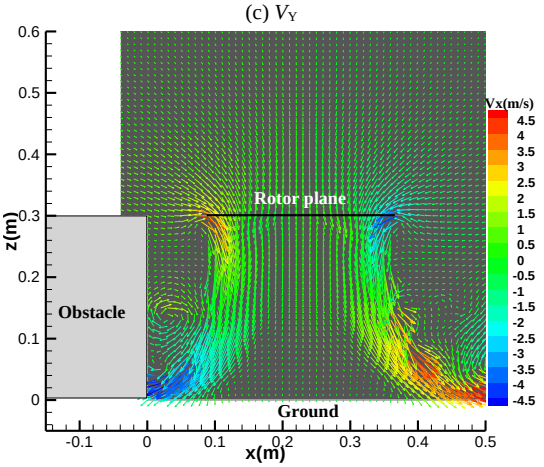

(d) Stream vector

Fig.14 Time averaged flow field of the rotor with the obstacle

Comparisons of the vertical velocity in the regions A and B at two distances above the ground are plotted in Fig.15. At the rotor plane, the velocity in the region A is identical to the region B. This is because the obstacle has small effect on the rotor plane. However, the velocity near the obstacle (r/R=1.5) in the region A is greater than that of the region B. This is a result of the recirculation produced by the interaction between the rotor wake and the obstacle.

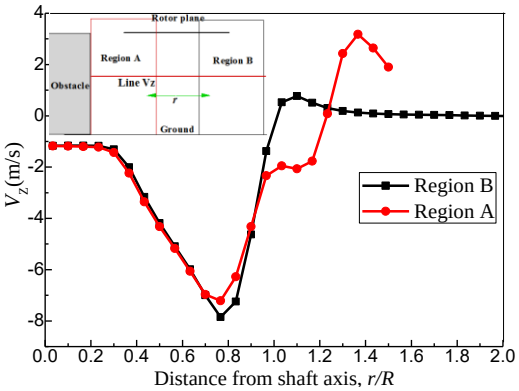

(a) Z=0.18m

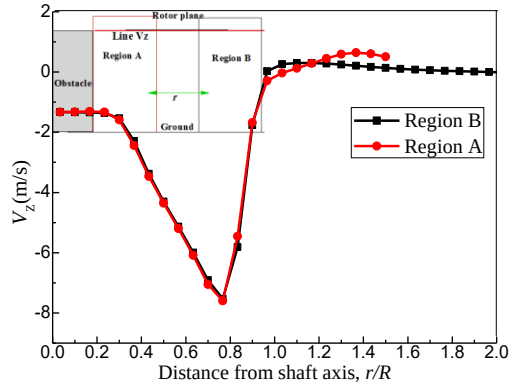

(b) Z=0.24m

Fig.15 V_Z velocity distribution parallel to the ground in the both regions

The comparison of the radial and vertical velocities at different locations in the regions A and B, shown in Fig. 16, provides some insight into the effect of the obstacle. Inner rotor regions (r=0.433R), the radial and vertical velocity profiles in the region A show similar trend as that of the region B as shown in Fig.16(c). However, contrary to the region B, the peak and its corresponding height of the radial velocity near the obstacle (r=1.1R) and away from it (r=0.833R) is smaller due to the barrier effect of the obstacle. Furthermore, because the interaction between the rotor wake and the obstacle yields a recirculation, as expected, the peak vertical velocity near the obstacle (r=1.1R) in the region A is greater than that of the region B as shown in Fig.16(a). Additionally, compared with the region B, slightly under the height corresponding to the peak velocity, the vertical velocity in the region A is larger due to the induced downwash of the recirculation.

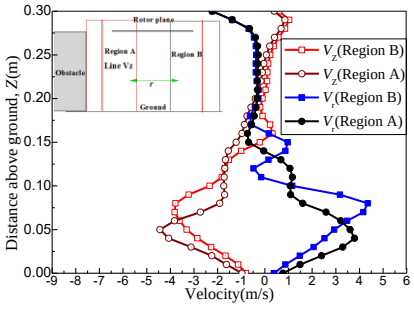

(a) r=1.1R

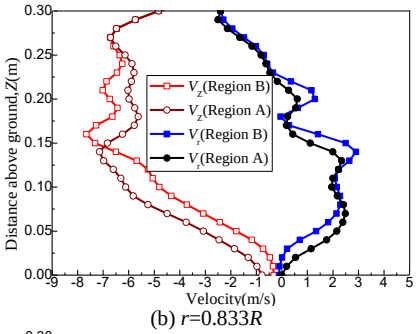

(b) r=0.833R

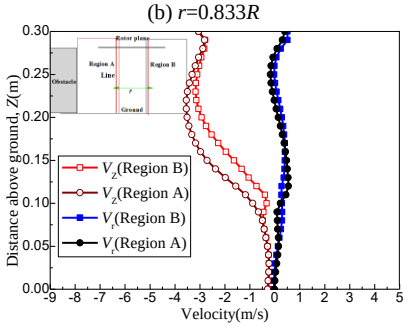

(c) r=0.433R

Fig.16 V_r velocity profiles normal to the ground on the both regions

Flow visualizations on the *XZ* and *YZ* planes are shown in Fig.17. As expected, similar to a single rotor in ground effect as shown in Fig.24(a), snapshots of the predicted rotor wake on the *YZ* plane in Fig.17(b) show the characteristic formation of the tip vortex and vortex sheet structures in the wake below the rotor, and the wall jet around the ground plane. However, as opposed to the *YZ* plane, a recirculation region is clearly observed on the *XZ* plane. The tip vortices are pushed up under the effect of the obstacle.

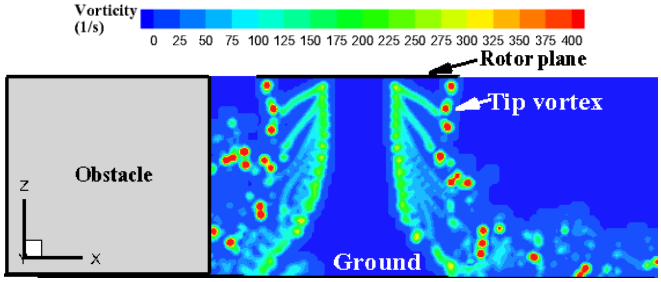

(a) *XZ* plane

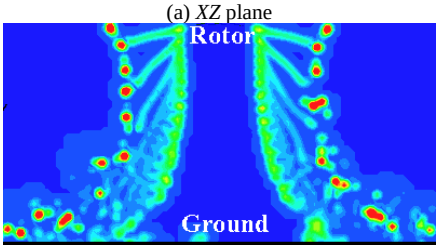

(b) *YZ* plane

Fig. 17 Flow visualization of the rotor wake

The time average flow field near the ground plane at Z=0.03m (*XY* plane) in Fig.18 provides further insight into the effect of the obstacle on the rotor wake. Compared with the region D, the radial velocity in the region C is smaller due to the blocking effect of the obstacle, while the tangential velocity close to and leave the obstacle is larger. Also worth noticing is that, Fig.18(b), the tangential velocity near the north and south surfaces of the obstacle are positive and negative, respectively, indicating that the flow moves toward to the obstacle. Furthermore, contrary to the flow leaving from the obstacle as shown in Fig.18(c), the velocity in the *X* direction close to the obstacle is faster due to the swirl resulting from the rotation. Moreover, the stagnation region on the surface of the obstacle is shown in Fig.18(d). This is also confirmed in Figures 18(a) and (c).

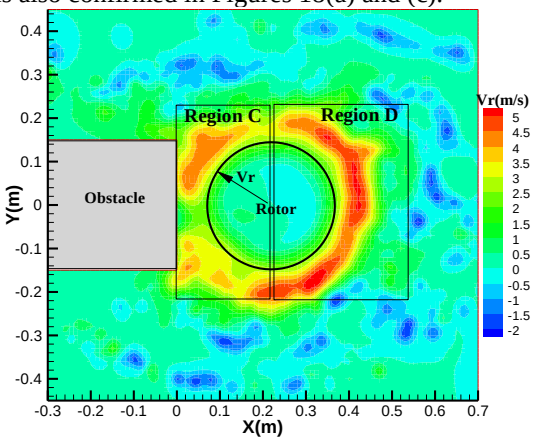

(a) V_r

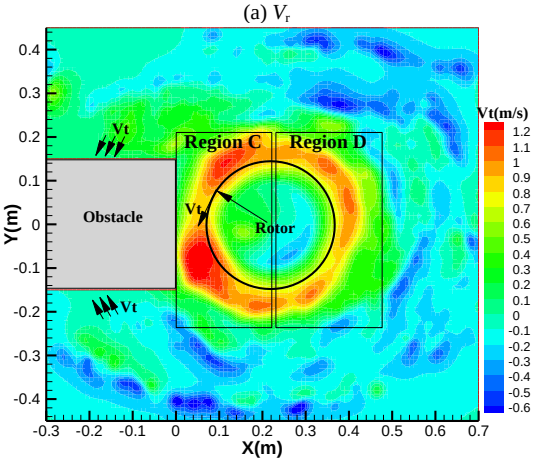

(b) V_t

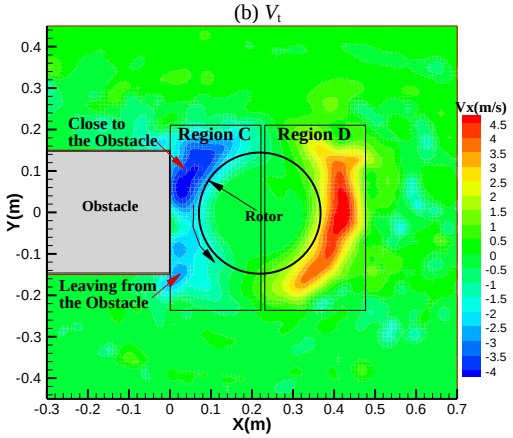

(c) V_X

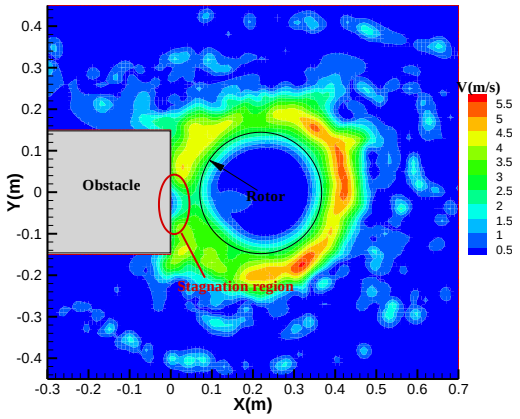

(d) V

Fig.18 Time averaged flow field at Z=0.03m

Difference of the Flow-Field between With and Without Obstacle

Figure 19 shows the comparison of V_X on the XZ plane of the rotor operating with and without the obstacle. Clearly, contrary to the flow field without the obstacle, shown in Fig.19(a), the outwash velocity in Fig.19(b) is smaller, and outwash and inflow are also observed in Fig.19(c) due to the recirculation region resulted from the strong interaction between the rotor wake and the obstacle. Furthermore, this is also confirmed in Fig.22(a), indicating that the interaction with the obstacle yields 21.6% and 23.3% decrease in the peak velocity and thickness of the outwash. Moreover, the comparison of V_Y of the rotor with and without the obstacle shows that, as opposed to the flow field without the obstacle, the velocity in the Y direction obviously changes from negative to positive, suggesting that there is a recirculation region near the obstacle. This phenomenon is also confirmed in Fig.22(b), which shows that the peak of velocity in the Y direction increases by 212.6% due to the interaction with the obstacle. Additionally, since the tip vortices expand as they approach the ground plane, there is a slightly up-wash near the ground. Conversely, the up-wash is obviously strengthened due to the effect of the obstacle. As a result, the up-wash and the downwash in the rotor wake slipstream produce the recirculation. Also, this process is confirmed in Fig. 22(c), which shows the vertical velocity profiles near the obstacle surface (X=0.01m). The obstacle causes an increase of 162.5% in the peak of the vertical velocity.

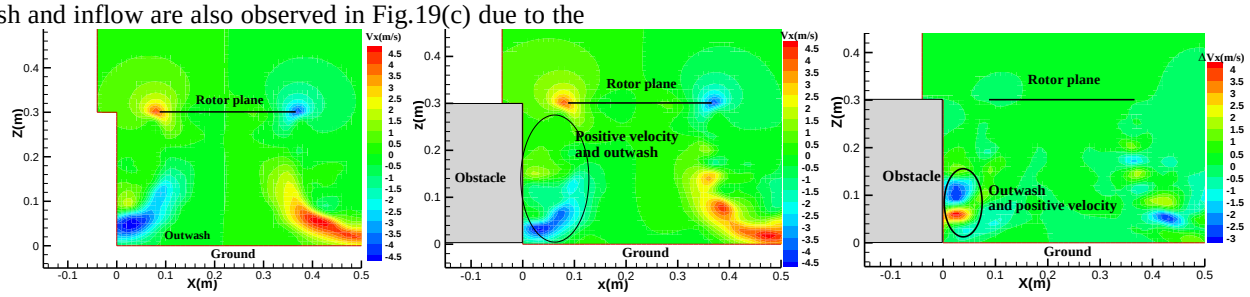

(a) Without obstacle (b) With obstacle (c) Difference

Fig.19 Comparison of V_X magnitude contours of the rotor with and without the obstacle

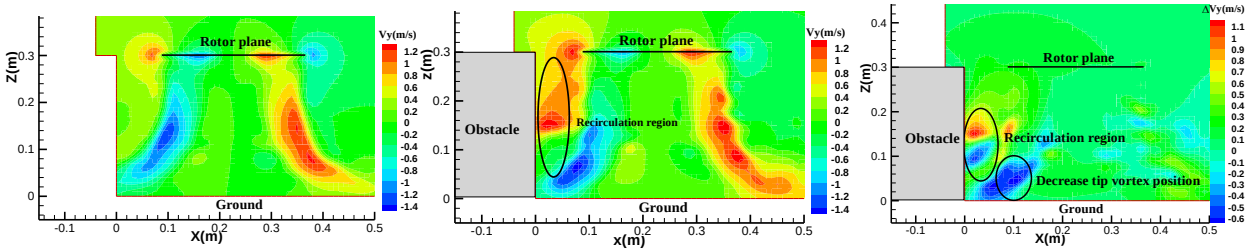

(a) Without obstacle (b) With obstacle (c) Difference

Fig.20 Comparison of V_Y magnitude contours of the rotor with and without the obstacle

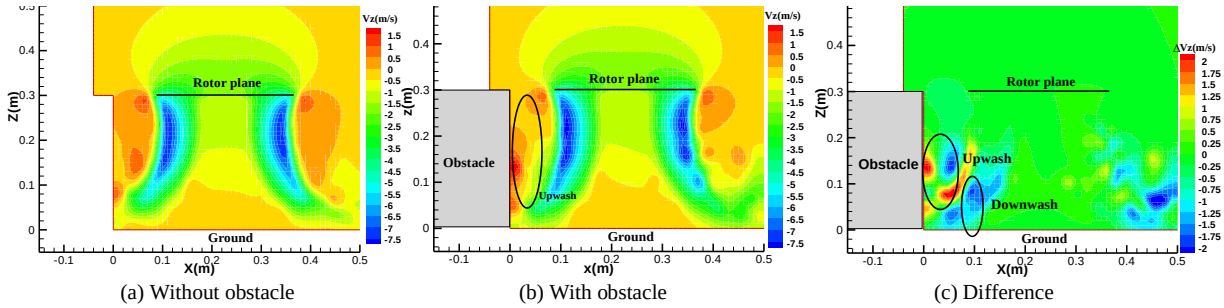

(a) Without obstacle (b) With obstacle (c) Difference

Fig.21 Comparison of V_Z magnitude contours of the rotor with and without the obstacle

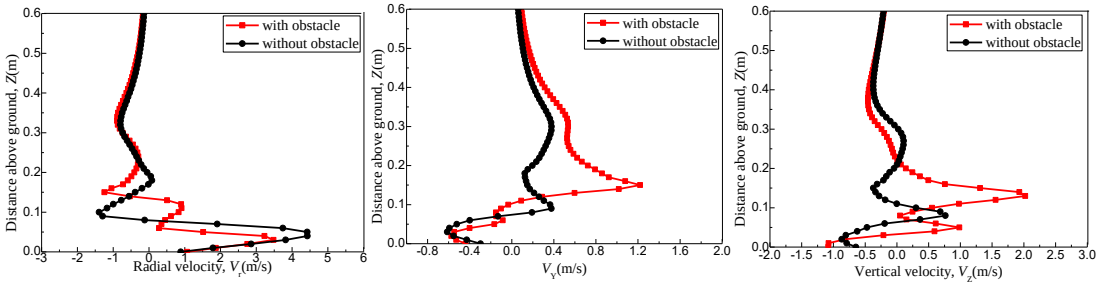

(a) V_r (b) V_Y (c) V_Z

Fig.22 Velocity profiles normal to the ground at X=0.01m with and without the obstacle

The wake structure of the rotor operating with and without the obstacle is plotted in Fig.23. The tip vortices of the rotor wake without the obstacle contract radially inwards, then expand radially outwards, and stretch as they approach the ground surface. However, they are blocked from convecting further by the obstacle, and climb and re-enter the rotor wake. This is confirmed in Fig.24, which shows the flow visualization of rotor wake with and without the obstacle.

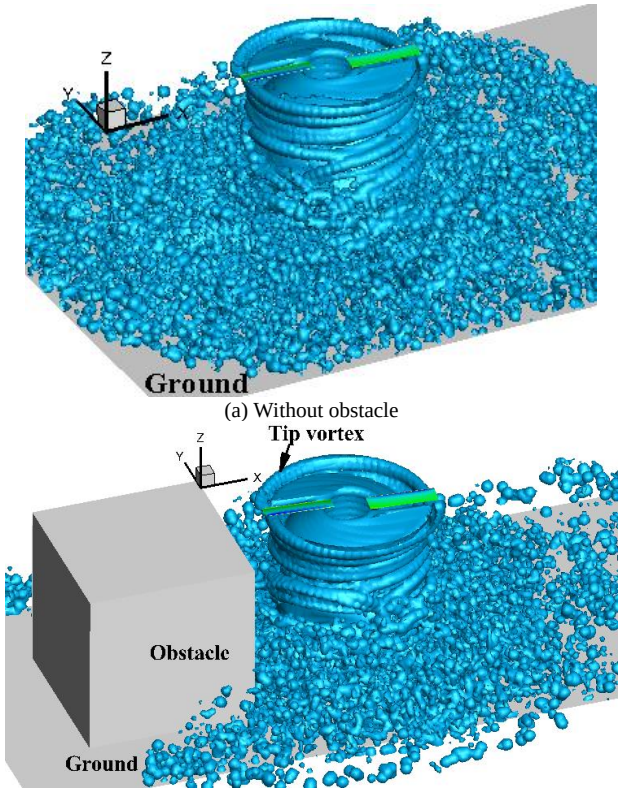

(a) Without obstacle

(b) With obstacle

Fig.23 Wake structure of the rotor with and without the obstacle

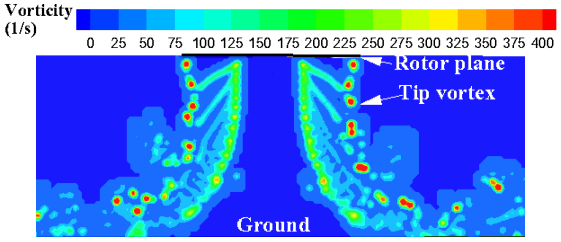

(a) Without obstacle

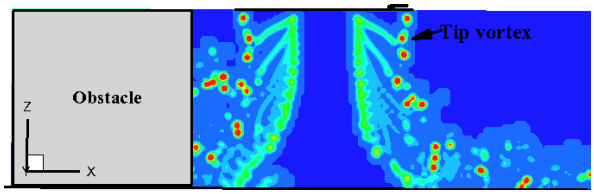

(b) With obstacle

Fig.24 Flow visualization of the rotor wake with and without the obstacle

Differences of the Flow-Field with Different Rotor Positions

The predicted velocity contours of the rotor at different positions are shown and compared with the experiment data in Figures 25-28 that also show the main features of the flow-field. The comparison demonstrates well correlation between the predictions and the measurements. Also, the velocity within the wake boundary and the radial outward expansion of the rotor induced flow are predicted reasonably well for a range of rotor positions, and the expansion is caused by the effect of the ground plane. Moreover, in all four cases, it is obvious that the rotor induced flow on the starboard side of the flow field is forced to expand radially outward as a wall jet. However, as expected, the wall jet near the obstacle is deflected by both the ground plane and the obstacle resulting in a recirculation region. This recirculation region is caused by the fact that the rotor wake, once deflected by the ground, is re-deflected again by the obstacle.

Clearly, as opposed to the rotor at Z=2.0R shown in Fig.26, the recirculation region due to the interaction between the wake and the obstacle is more prominent and the layer is thicker and faster at Z=1.5R, *as* shown in Fig.25. In addition, the rotor wake impinges upon the ground plane before being deflected by the obstacle at X=2.0R and 3.0R shown in Fig.27 and Fig.28. However, the rotor slipstreams at X=1.5R shown in Fig.26 impinges directly upon the obstacle rather than the ground plane. This is because the expansion flow of the rotor wake is closed to the obstacle. Furthermore, the layer that goes upwards close to the obstacle is faster as the position of the rotor decreasing, indicating a stronger interaction.

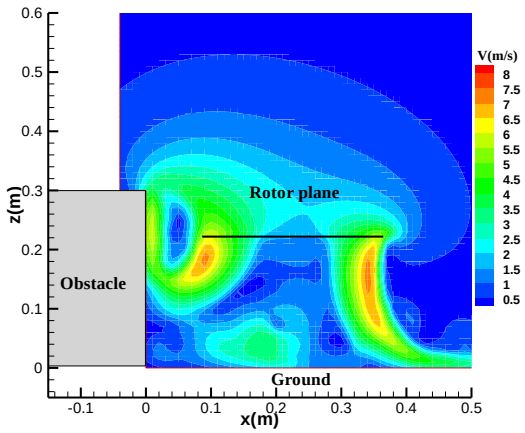

(a) Prediction

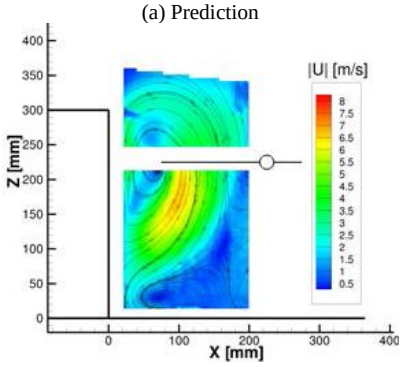

(b) Experiment[8]

Fig.25 Velocity magnitude contours of the rotor at *Z*=1.5*R*, *X*=1.5*R*

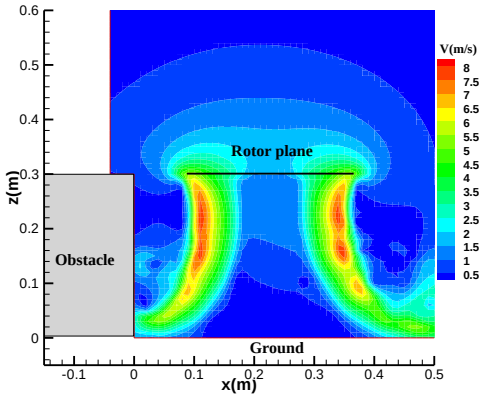

(a) Prediction

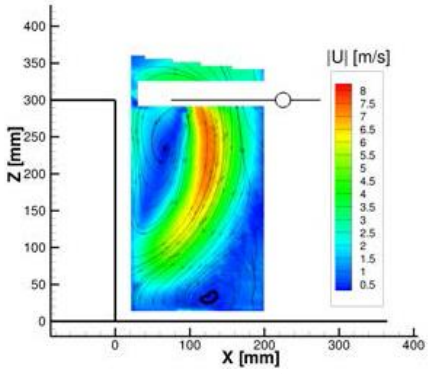

(b) Experiment[8]

Fig.26 Velocity magnitude contours of the rotor at *Z*=2.0*R*, *X*=1.5*R*

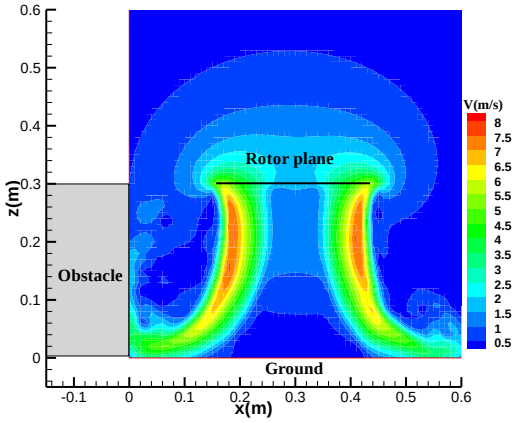

(a) Prediction

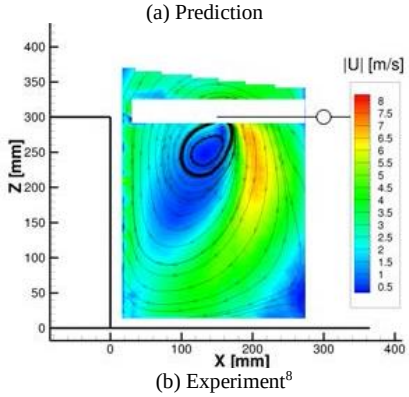

(b) Experiment[8]

Fig.27 Velocity magnitude contours of the rotor at *Z*=2.0*R*, *X*=2.0*R*

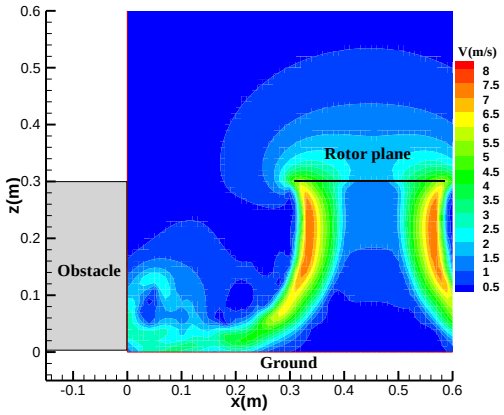

(a) Prediction

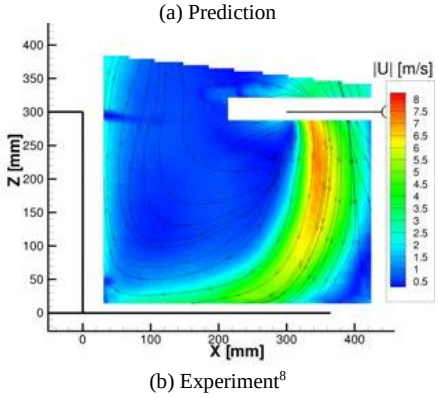

(b) Experiment[8]

Fig.28 Velocity magnitude contours of the rotor at *Z*=2.0*R*, *X*=3.0*R*

Figure 29 shows wake structure of the rotor operating at different positions with respect to the obstacle. Compare to

the X=3R, the rotor wake at the X=1.5R shown in Fig.29(b) twines around the obstacle and stretch more intensely. In addition, as the rotor position in X direction increases, the interaction between the vortex and the obstacle, and the stretching of vortices are weakened. The predicted flow visualization of the rotor wake under the interaction of the ground plane and the obstacle is shown in Fig. 30 to highlight the structures found within the wake near the obstacle in Fig.29. Snapshots of the predicted flow fields show that the tip vortex near the obstacle is clearly reflected and pushed upward by the obstacle and the ground plane resulting in vortex pairing and a recirculation in all cases. Compared the height of involved tip vortex of the rotor at Z=2.0R shown in Fig.30(b), the position of the reflected tip vortices is higher than the rotor plane at Z=1.5R shown in Fig.30(a) indicating that the interaction between the tip vortices and the obstacle is intense and the recirculation is strengthened. However, the height of the involved tip vortices decreases with increasing the rotor position in the X direction as shown in Fig. 30(b)-(d). This is because the tip vortices will be first reflected by the ground plane and then re-deflected again by the obstacle. As a result, the recirculation region is smaller, and the interaction of vortex-obstacle is weakened.

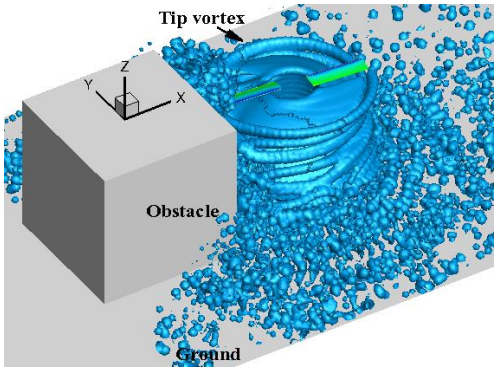

(a) Z=1.5R, X=1.5R

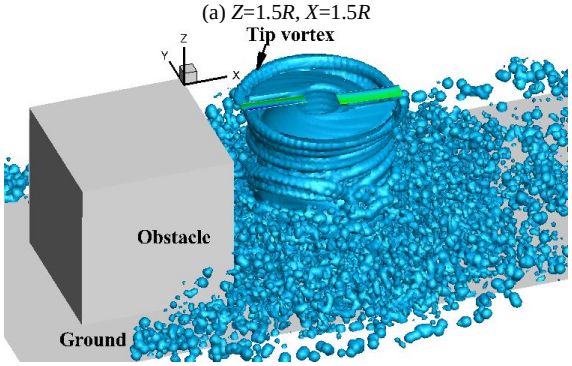

(b) Z=2.0R, X=1.5R

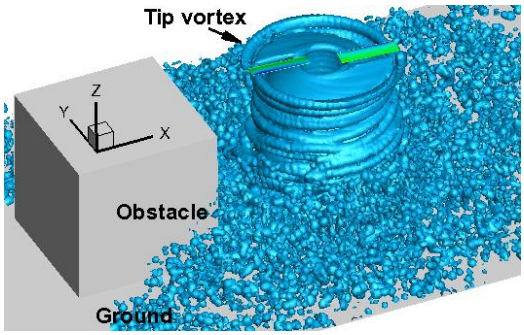

(c) Z=2R, X=2R

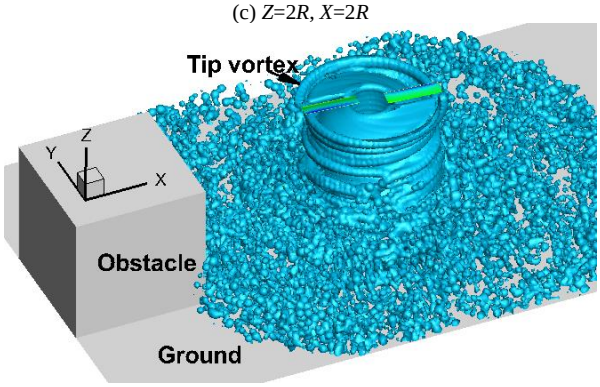

(d) Z=2R, X=3R

Fig.29 Wake structure of the rotor at different positions with respect to the obstacle

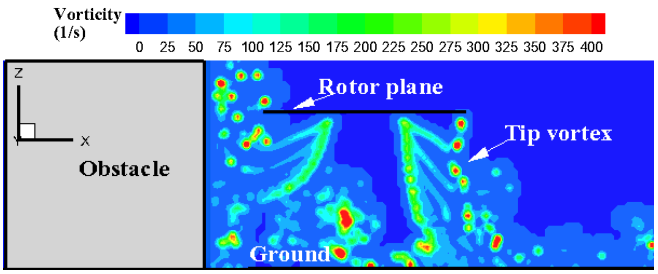

(a) Z=1.5R, X=1.5R

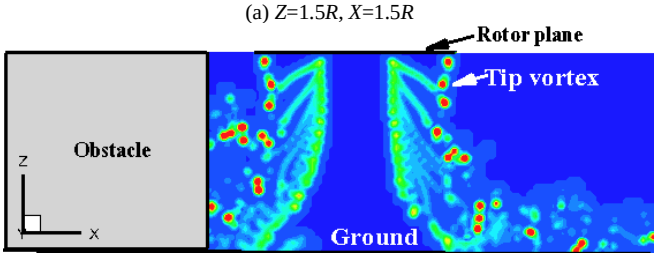

(b) Z=2.0R, X=1.5R

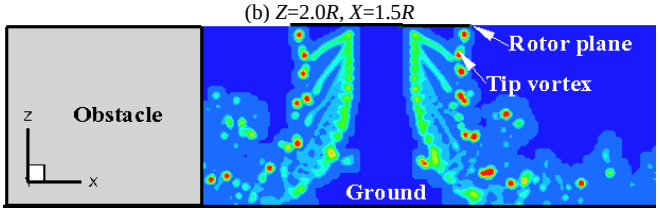

(c) Z=2R, X=2R

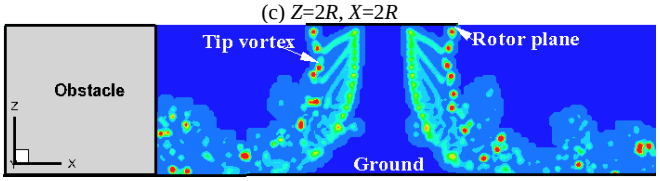

(d) Z=2R, X=3R

Fig.30 Flow visualization of the rotor wake at different positions with respect to the obstacle

Rotor Thrust and Pressure of the Rotor-Ground-Obstacle

Figure 31 show the variation of thrust coefficient of the "Wee" rotor with different positions respect to the obstacle. It is shown that the predicted ratio between C_T and $C_{T,OGE}$ is found to match very well with the experimental data[8]. The rotor thrust coefficient at X=4.0R, Z=4.0R is equal to that of OGE case since the rotor is far away from the obstacle and the ground, whereas it at X=4.0R, Z=3.0R is greater than that of OGE as it is influenced by the ground effect. As the position of the rotor in X direction decreases, the rotor thrust at Z=3.0R and 4.0R increases. This is because the effect of the obstacle is strengthened with decreasing the position of the rotor in X direction. Furthermore, the increase of the rotor thrust due to the ground without the obstacle are 4% and 20% when the rotor is running at distance above the ground at Z=1.0R and 2.0R. Particularly, the ratio between C_T and $C_{T,OGE}$ are about 1.04 at Z=3.0R and 1.195 at Z=4.0R, respectively, which are similar to that of the rotor operating in ground effect at Z=1.0R and Z=2.0R. This indicates that when the rotor is located over the centre of the obstacle, the effect of the obstacle is similar to that of the ground. Moreover, as the rotor is positioned outwards from the centre of the obstacle, the rotor thrust is reduced quickly since the rotor wake convects far away from the obstacle as shown in Fig.7(d) and the induced inflow increases as shown in Fig.6(b). Additionally, it is interesting to note that the rotor thrust at X=1.0R, Z=3.0R is less than that of OGE which is also observed in the experiment and indicates the strong effect of the obstacle. This can be explained by the development of a small recirculation region where the rotor wake is first reflected by the ground plane, and re-deflected again by the obstacle, and then re-inject into the rotor wake as mentioned before.

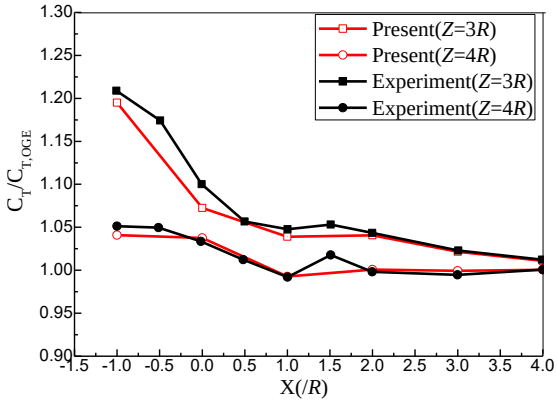

Fig.31 Rotor thrust at different positions with respect to the obstacle

Comparisons of the pressure on the obstacle up surface with experiment when the rotor is located at X=-1.0R, Z=3.0R are plotted in Fig.32. It is shown that the predicted pressure distribution shows similar trend as the experiment. The pressure at the edge of the box, compared to the centre of the box is greater since the rotor wake impinges directly on the edge of the box as shown in Fig.7(b). Furthermore, the pressure at the vertex of the obstacle is smaller than that of the edge due to the rotor wake convects downstream around the vertex. The extracted pressure at X=-0.01967m, X=-0.2754m, Y=-0.127m, and Y=0.127m, across the obstacle surface for this configuration are shown in Fig.33. Also, experimental data are used to validate the present approach. In general, there is an agreement between the computational and the experimental results in X and Y directions. Furthermore, contrary to the both sides, the pressure at the centre in Fig.33 is comparable and even predominant, which is also observed at the experiment. Additionally, even though there are small discrepancies, the overall comparison is still good.

The predicted distribution of the pressure on the obstacle surface when the rotor is located at X=0.0R, Z=3.0R is compared with experiments as shown in Fig.34. It is shown that even through the predicted peak pressure is slightly under-predicted, whereas the increase of the pressure at the centre of the obstacle is captured. Furthermore, contrary to the X=-1.0R, the peak of the pressure is pushed towards the centre of the obstacle since the rotor wake impinges upon the centre of obstacle as shown in Fig.7(d). A more quantitative validation of the present method compares the pressure profiles at different locations (Y=-0.127m, 0.0m, 0.0944m, and 0.127m) with the experimental data as shown in Fig.35. The overall pressure distribution is well predicted at different Y position. Moreover, the peak of the pressure is slightly smaller than that of the experiment, while the increase of the pressure is found to match well with the experimental data.

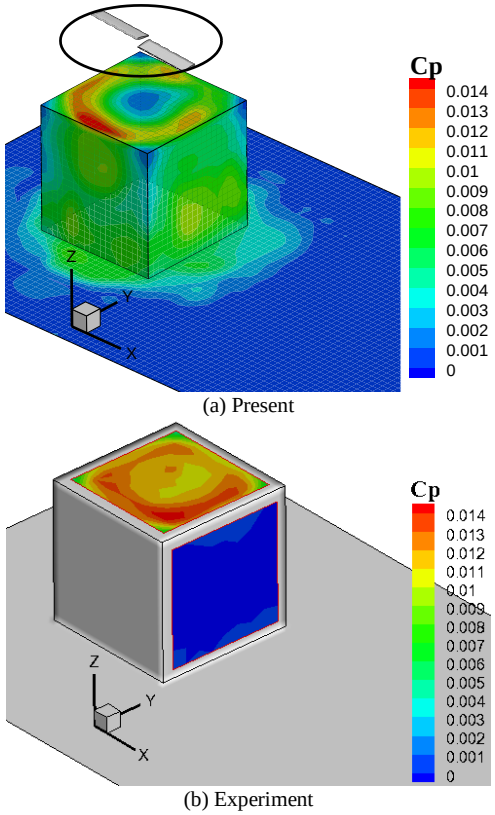

(a) Present

(b) Experiment

Fig.32 Pressure coefficient on the obstacle. The rotor is located at station A (X=-1.0R, Z=3.0R).

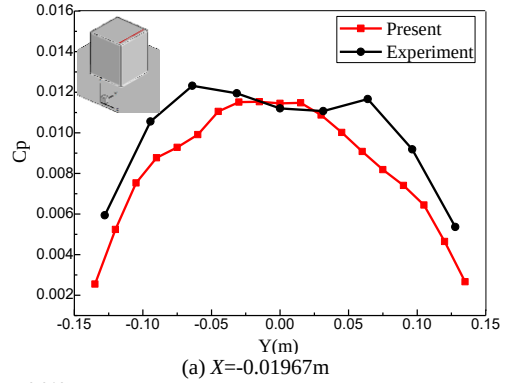

(a) X=-0.01967m

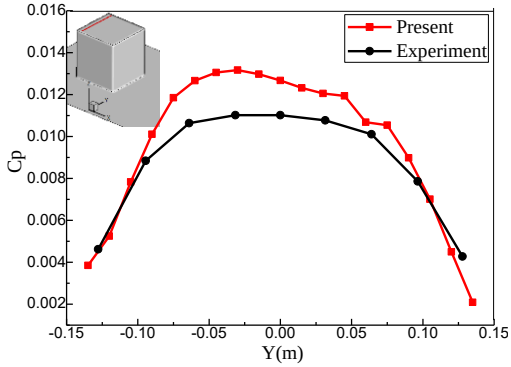

(b) X=-0.2754m

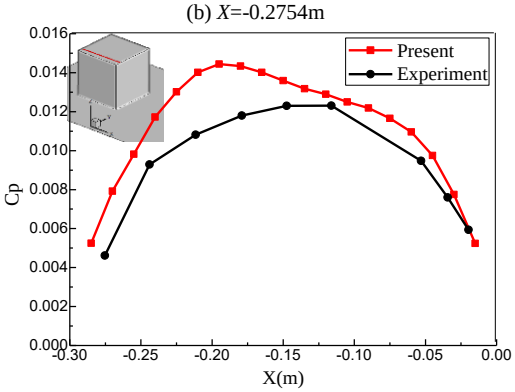

(c) Y=-0.127m

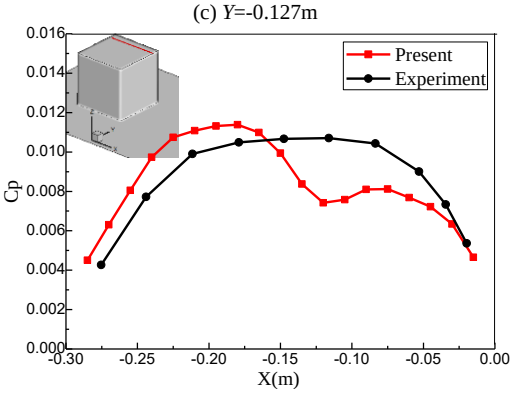

(d) Y=0.127m

Fig.33 Pressure coefficient on the obstacle in X and Y directions. The rotor is located at station A (X=-1.0R, Z=3.0R).

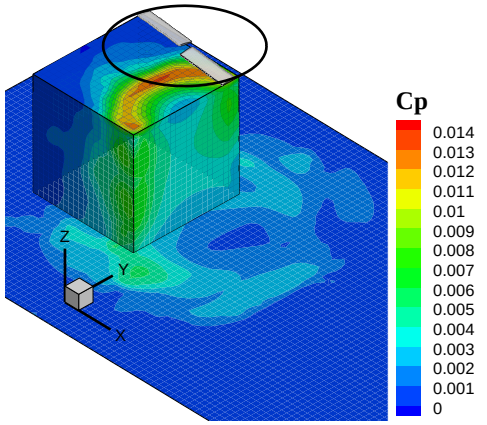

(a) Present

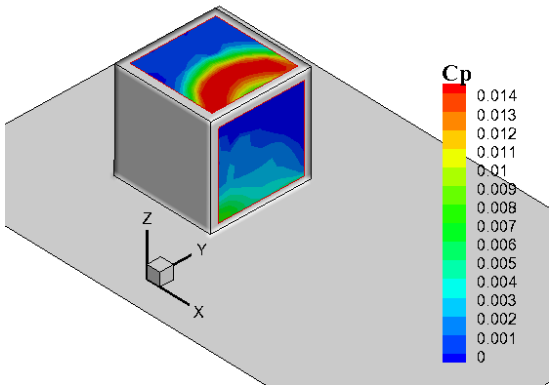

(b) Experiment

Fig.34 Pressure coefficient on the obstacle. The rotor is located at station B (X=0.0R, Z=3.0R).

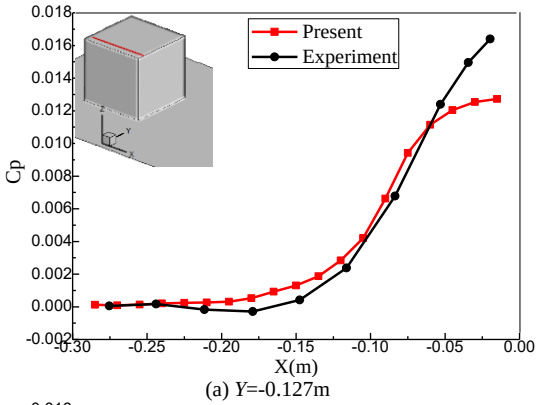

(a) Y=-0.127m

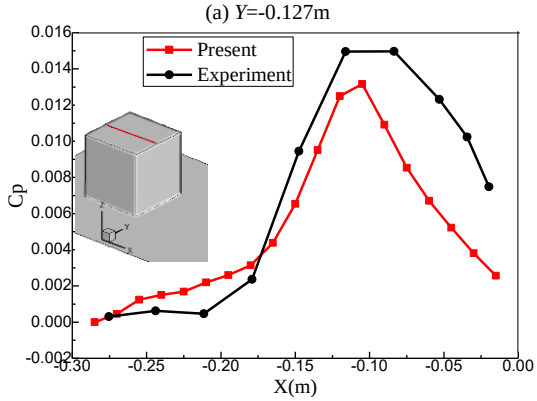

(b) Y=0.0m

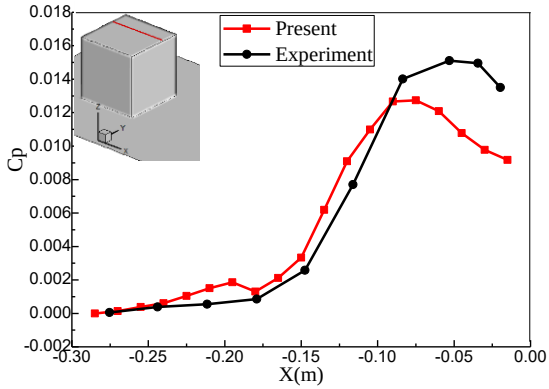

(c) Y=0.09443m

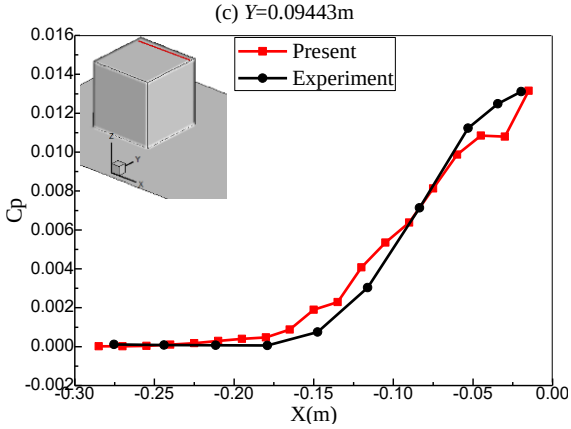

(d) Y=0.127m

Fig.35 Pressure coefficient on the obstacle in *Y* direction. The rotor is located at station B (*X*=0.0*R*, *Z*=3.0*R*).

Differences of the Rotor Force with Different Rotor Positions

Figure 36 shows the rotor thrust, roll and pitch moments for the rotor at different positions with respect to the obstacle (Z=2.0R). Even through the rotor is running without the obstacle, there are fluctuations of the rotor thrust, roll and pitch moments. This is because the flow field is also unsteady due to the effect of the ground. However, contrary to the case without obstacle, the fluctuations of the rotor thrust, roll and pitch moments under the effect of the obstacle are obviously strengthened. Furthermore, as the distance between the rotor and the obstacle increases, the peak-to-peak of the thrust, and the average and peak-to-peak values of the roll and pitch moments decrease, while the average of the thrust increases. It is shown that when the rotor position is larger than 3R away from the obstacle in the X direction, the variations of the thrust, roll and pitch moments are similar to the isolated rotor case.

The thrust, roll and pitch moments for the rotor at different distances above the ground (X=2.0R) are plotted in Fig.37. Like for the out of ground effect (OGE) cases, the variation of the rotor thrust, roll and pitch moments at Z=4.0R are small. Furthermore, like for the previous cases at different positions (Z=2.0R), when the distance above the ground is larger than 3R, the variations of the thrust, roll and pitching moment are similar to the OGE. However, the fluctuations of the thrust, roll and pitch moments at Z=1.0R and 1.5R are clearly strengthened, and the average of the thrust and roll moment increase, while the average of the pitching moment decreases. The negative sign of the pitch moment indicates a rotor nose-down attitude, suggesting that the rotor will be pulled towards the obstacle. This is because the effect of the ground increases the rotor thrust, and the obstacle changes the rotor inflow yielding stronger fluctuations of the thrust, roll and pitch moments.

The distributions of the rotor thrust, roll and pitching moments for the rotor at different positions are shown in Fig.38 that provides further insight into the effect of the obstacle. In area C, the average of the thrust is strengthened and is larger than for OGE by 27.2% due to the effect of the ground. In area A it also increases by 18.1% due to the effect of the obstacle. Compared with area C, the average thrust in the area A is smaller because the rotor wake twines around the obstacle as shown in Figure 7(a) and (b). However, contrary to both areas A and C, the thrust in area B decreases, and is smaller than OGE by 16.0%. The reason for the difference can be understood by comparing the inflow in Figures 25 and 28. There is a strong recirculation between the rotor and the obstacle at X=1.5R, Z=1.5R, which obviously decreases the blade thrust. Furthermore, the peak-to-peak values of the roll and pitch moments clearly increase due to the effect of the obstacle, which will result in stronger rotor vibrations.

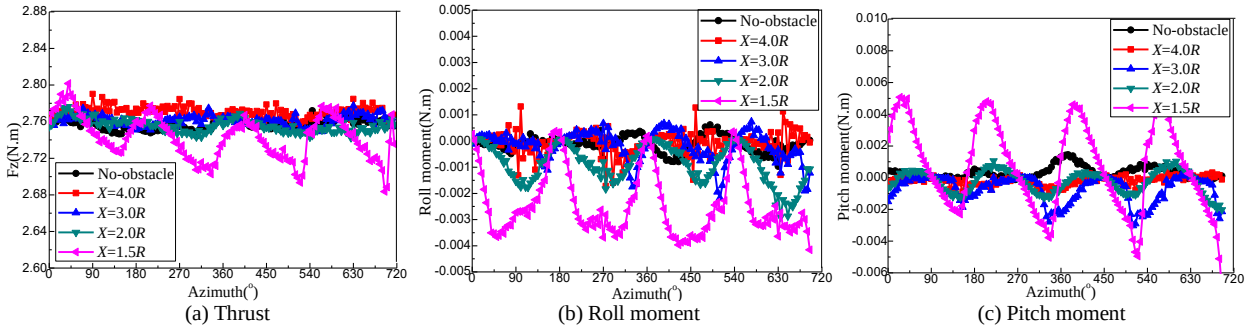

(a) Thrust (b) Roll moment (c) Pitch moment

Fig.36 Thrust, roll and pitch moment for the rotor at different positions with respect to the obstacle (*Z*=2.0*R*)

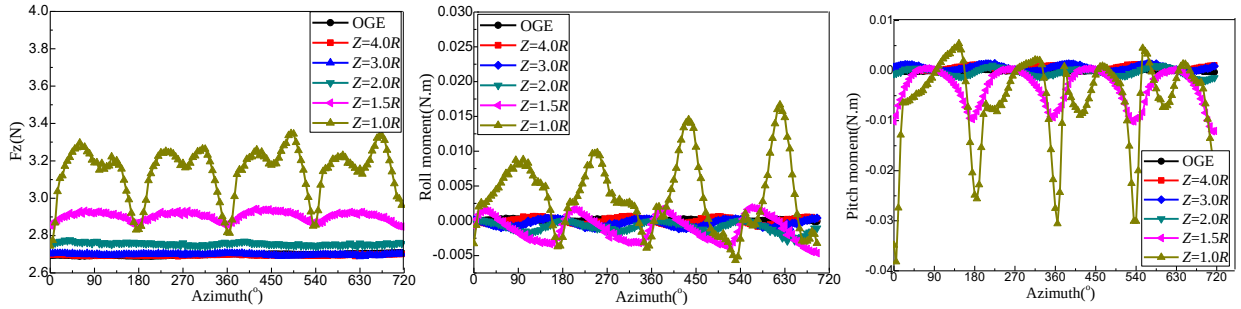

(a) Thrust (b) Roll moment (c) Pitch moment

Fig.37 Thrust, roll and pitch moment for the rotor at different positions with respect to the obstacle (*X*=2.0*R*)

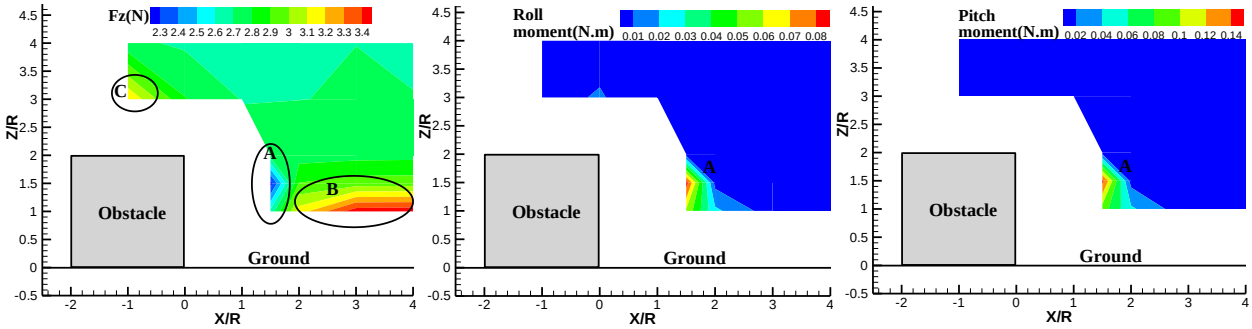

(a) Average of thrust (b) Peak-to-peak of roll moment (c) Peak-to-peak of pitch moment

Fig.38 Distribution of the thrust, roll and pitch moment for the rotor at different positions

CONCLUSIONS

A vortex-based approach is used here to predict the flow-field of a rotor operating near ground and obstacles. The aerodynamics of the rotor is modelled using an unsteady panel method, and the unsteady behavior of the rotor wake is taken into account through the employed vortex particle method. The effect of the ground and the obstacle are modelled by a viscous boundary model. The present approach is applied to a scaled-rotor, including a "Larger" and a "Wee" configurations. Experiments by the University of Glasgow were used, and some conclusions can be drawn as following:

(1) The predicted rotor-induced flow under the aerodynamic interaction between the rotor and the ground obstacle compared reasonably well with the experiments in terms of magnitude and phase, and the peak velocity of the radial outwash and vertical downwash were predicted correctly.

(2) The tip vortices were pushed upwards and re-entered the rotor wake resulting in a recirculation region between the rotor wake and obstacle.

(3) Contrary to the case without the obstacle, the peak value and thickness of the radial outwash near the obstacle is smaller due to blockage effects, and up-wash is also observed.

(4) As the rotor closes to the obstacle, the rotor slipstreams impinge directly on the obstacle surfaces. The up-wash near the obstacle is faster as the distance to the rotor decreases, indicating a stronger interaction between the rotor wake and the obstacle.

(5) Contrary to the case without obstacle, the fluctuations of the rotor thrust, roll and pitch moments are. When the distance between the rotor and the obstacle is larger than 3*R*, the effect of the obstacle is small.

Author contact: JianfengTan Jianfengtan@njtech.edu.cn
George N. Barakos George.Barakos@glasgow.ac.uk.

ACKNOWLEDGMENTS

This work was supported by the National Natural Science Foundation of China (Grant No. 11502105), and the support of Natural Science Foundation of Jiangsu Province (Grant No. BK20161537) and the Jiangsu Government Scholarship for Overseas Studies were gratefully acknowledged. The use of the data of the experiments by Zagaglia et al. in Ref.8 was also gratefully acknowledged. Also, this work was part of the GARTEUR-AG22 research on the wake interaction with the building.

REFERENCES

[1]U.S. Joint Helicopter Safety Analysis Team. "The Compendium Report: The U.S. JHAST Baseline of Helicopter Accident Analysis, Volume I." The International Helicopter Safety Team, 2011.

[2]Timm, G. K. "Obstacle-Induced Flow Recirculation." *Journal of American Helicopter Society*, Vol.10, (4), 1965, pp: 5-24.

[3]Lusiak, T., Dziubinski, A., Szumanski, K. "Interference between Helicopter and Its Surroundings, Experimental and Numerical Analysis." *Task Quarterly*, Vol.13, (4), 2008, pp: 379-392.

[4]Quinliven, T. A., Long, K. R. “Rotor Performance in the Wake of a Large Structure.” *Presented at the American Helicopter Society 65th Annual Forum*, AHS, Grapevine, Texas, 2009, pp: 447-475.

[5]Polsky, S. A., Wilkinson, C. H. “Computational Study of Outwash for a Helicopter Operating Near a Vertical Face with Comparison to Experimental Data.” *AIAA Modeling and Simulation Technologies Conference*, AIAA, Chicago, Illinois, 2009.

[6]Sanka, L. “Ground Effect of a Rotor Hovering Above a Confined Area.” *Frontiers in Aerospace Engineering*, Vol.3, (1), 2014, pp: 7-16.

[7]Gibertini, G., Grassi, D., Parolini, C., Zagaglia, D., Zanotti, A. “Experimental Investigation on the Aerodynamic Interaction between a Helicopter and Ground Obstacles.” *Proc IMechE Part G: J Aerospace Engineering*, Vol. 229, (8), 2015, pp: 1395-1406.

[8]Zagaglia, D., Giuni, M., Green, R. B. “Rotor-Obstacle Aerodynamic Interaction in Hovering Flight: an Experimental Survey.” *Presented at the AHS 72nd Annual Forum*, AHS, West Palm Beach Florida, 2016, pp: 356-364.

[9]Alpman, E., Long, L. N., Bridges, D. O., Horn, J. F. “Fully-Coupled Simulations of the Rotorcraft/ Ship Dynamic Interface.” *Presented at the American Helicopter Society 63rd Annual Forum*, AHS, Virginia Beach, VA, 2007, pp: 1552-1567.

[10]Gibertini, G., Droandi, G., Zagalia, D., Antoniazza, P., Catelan, A. O. “CFD Assessment of the Helicopter and Ground Obstacles Aerodynamic Interference.” *42nd European Rotorcraft Forum*, ERF, Lille, France, 2016, pp: 553-556.

[11]Chirico, G., Szubert, D., Vigevano, L., Barakos, G. N. “Numerical Modelling of the Aerodynamics Interference between Helicopter and Ground Obstacles.” *CEAS Aeronaut J*. 2017, pp: 1-23..

[12]Schmid, M. “Simulation of Helicopter Aerodynamics in the Vicinity of an Obstacle Using a Free Wake Panel Method.” *43rd European Rotorcraft Forum*, ERF, Milan, Italy, 2017.

[13]Tan, J. F., and Wang, H. W. “Simulating Unsteady Aerodynamics of Helicopter Rotor with Panel/Viscous Vortex Particle Method.” *Aerospace Science and Technology*, Vol. 30, (1), 2013, pp: 255-268.

[14]Safety and Airspace Regulation Group, “Manual of Air Traffic Services – Part 1, CAP 493”, The UK Civil Aviation Authority, 2015.

[15]Degond, P. S., and Gallic, M. “The Weighted Particle Method for Convection-Diffusion Equations. Part 1. the Case of an Isotropic Viscosity.” *Math. Comp*, Vol. 53, 1989, pp: 485- 507.

[16]Degond, P. S., and Gallic, M. “The Weighted Particle Method for Convection-Diffusion Equations. Part 2. the Anisotropic Case.” *Math. Comp*, Vol. 53, 1989, pp: 509- 525.

[17]Cottet, G. -H., and Koumoutsakos, P. *Vortex Methods, Theory and Practice*, Cambridge University Press, Cambridge, 2000.

18Koumoutsakos, P., Leonard, A., and Pepin, F. “Boundary Conditions for Viscous Vortex Method.” *Journal of Computational Physics*, Vol.113, 1994, pp: 52-61.

19Ploumhans, P., Daeninck, G., and Winckelmans, G. “Simulation of Three-dimensional Bluff-body Flows Using the Vortex Particle and Boundary Element Methods.” *Flow, Turbulence and Combustion*, Vol. 73, 2004, pp: 117-131.

[20]Poncet, P. “Topological Aspects of Three-dimensional Wakes Behind Rotary Oscillating Cylinders.” *Journal of Fluid Mechanics*, Vol. 517, 2004, pp: 27-53.

[21]Ploumhans, P., and Winckelmans, G. S. “Vortex Methods for High-resolution Simulations of Viscous Flow Past Bluff Bodies of General Geometry.” *Journal of Computational Physics*, Vol. 165, 2000, pp: 354-406.

[22]Ploumhans, P., Winckelmans, G. S., Salmon, J. K., Leonard, A., and Warren, M.S. “Vortex Methods for Direct Numerical Simulation of Three-Dimensional Bluff Body Flow: Application to the Sphere at *R*e=300, 500, and 1000.” *Journal of Computational Physics*, Vol. 178, 2002, pp: 427-463.